PHYSICAL REVIEW E

STATISTICAL PHYSICS, PLASMAS, FLUIDS, AND RELATED INTERDISCIPLINARY TOPICS

THIRD SERIES, VOLUME 60, NUMBER 6 PART B DECEMBER 1999

ARTICLES

Eutectic colony formation: A stability analysis

Mathis Plapp and Alain Karma

Physics Department and Center for Interdisciplinary Research on Complex Systems, Northeastern University, Boston, Massachusetts 02115

(Received 28 December 1998; revised manuscript received 9 April 1999)

Experiments have widely shown that a steady-state lamellar eutectic solidification front is destabilized on a scale much larger than the lamellar spacing by the rejection of a dilute ternary impurity and forms two-phase cells commonly referred to as ''eutectic colonies.'' We extend the stability analysis of Datye and Langer [V. Datye and J. S. Langer, Phys. Rev. B **24**, 4155 (1981)] for a binary eutectic to include the effect of a ternary impurity. We find that the expressions for the critical onset velocity and morphological instability wavelength are analogous to those for the classic Mullins-Sekerka instability of a monophase planar interface, albeit with an effective surface tension that depends on the geometry of the lamellar interface and, nontrivially, on interlamellar diffusion. A qualitatively new aspect of this instability is the occurrence of oscillatory modes due to the interplay between the destabilizing effect of the ternary impurity and the dynamical feedback of the local change in lamellar spacing on the front motion. In a transient regime, these modes lead to the formation of large scale oscillatory microstructures for which there is recent experimental evidence in a transparent organic system. Moreover, it is shown that the eutectic front dynamics on a scale larger than the lamellar spacing can be formulated as an effective monophase interface free boundary problem with a modified Gibbs-Thomson condition that is coupled to a slow evolution equation for the lamellar spacing. This formulation provides additional physical insights into the nature of the instability and a simple means to calculate an approximate stability spectrum. Finally, we investigate the influence of the ternary impurity on a short wavelength oscillatory instability that is already present at off-eutectic compositions in binary eutectics.
[S1063-651X(99)18010-3]

PACS number(s): 81.30.Fb, 64.70.Dv

I. INTRODUCTION

The interfacial patterns that arise naturally during the solidification of eutectic alloys have attracted widespread interest for several decades from both fundamental and practical viewpoints. At a fundamental level, the main theoretical challenge lies in understanding the complex spatiotemporal dynamics of phase boundaries (solid-liquid and solid-solid) resulting from the competition of two thermodynamically stable solid phases growing simultaneously into a metastable liquid phase. In particular, one basic question is how to understand the nature of the morphological instability of the simplest spatially periodic steady state that gives rise to this rich dynamics. From a practical viewpoint, the composite microstructure formed by lamellae or rods of these two solid phases growing simultaneously from the melt leads to interesting materials where the properties of two different solids can be advantageously combined. Moreover, the typical size of the microstructure pattern is about an order of magnitude smaller than in dendritic alloys, leading to superior mechanical properties. Consequently, understanding the solidification processing conditions that yield a particular eutectic microstructure is a goal of direct technological relevance.

Since the early investigations of eutectic alloys, it has been remarked that besides the fine lamellae or rods, there may exist cellular structures, termed colonies [1–9]. Their size is typically 10 to 100 times the lamellar spacing. In Fig. 1 we show an experimental picture of colonies obtained in a directional solidification experiment [4]. In their overall shape, the two-phase cells are remarkably similar to the monophase (i.e., single solid phase) solidification cells formed in standard directional solidification of a dilute binary alloy. This analogy is further supported by the experimental finding that colonies appear only when a ternary impurity, rejected by both solid phases, is present [2,8]. In contrast, in binary eutectics the large scale solidification front stays planar for a range of compositions around the eutectic point. This suggests that the mechanism of the insta-

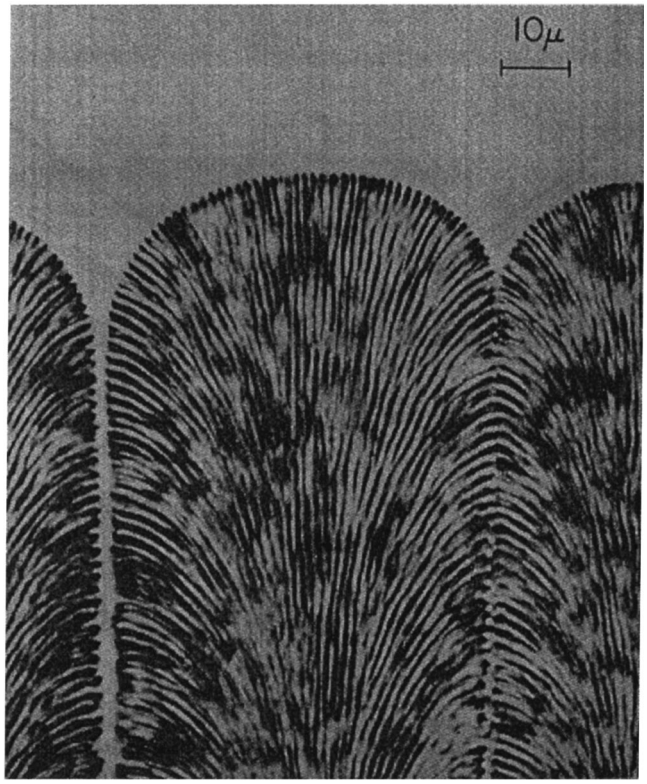

FIG. 1. Eutectic colonies in the transparent organic alloy CBr_4-C_2Cl_6 (from Ref. [4]), grown by a directional solidification experiment. The growth direction is from bottom to top. The envelope of this two-phase structure (i.e., the solidification front on a scale much larger than the lamellar spacing) closely resembles the typical monophase cells observed during the directional solidification of a dilute binary alloy.

bility is similar to the classical Mullins-Sekerka instability of a monophase solidification front [10]. Indeed, its onset is relatively well described quantitatively by the constitutional supercooling criterion [11], according to which the interface becomes unstable when the ternary impurity concentration gradient in the liquid ahead of the interface exceeds a critical value set by the ratio G/v_p of the temperature gradient and the pulling speed of the sample. However, the spatiotemporal character of the linear modes associated with this instability has never been investigated. In particular, it has remained unclear how the Mullins-Sekerka analysis has to be modified to account for the composite structure of the interface. To answer this question, we present in this paper a linear stability analysis of a lamellar eutectic solidification front in the presence of a ternary impurity.

It is useful to first briefly review the progress accomplished to date on the related problem of binary eutectic stability (without a ternary impurity). The approach that we shall adopt here builds on earlier work in this context. Theoretical developments have mostly focused on the lamellar morphology in thin-film geometry, as then the problem can be treated as quasi-two-dimensional. For a stability analysis, one must first obtain a steady-state solution: a shape-preserving solidification front propagating at constant velocity. Studies of this problem [11–15] led to the insight that there exists a family of steady-state solutions that can be parametrized by the lamellar spacing λ. The average undercooling ΔT of the solid-liquid interface with respect to the eutectic temperature depends on λ, and the curve ΔT versus λ presents a minimum for a certain spacing $\lambda_{\min}$. The experimentally observed spacings are usually close to $\lambda_{\min}$ [16].

A hypothesis attributed to Cahn by Jackson and Hunt [15] is that the lamellae always grow normal to the envelope of the solidification front. This hypothesis seems to work well in practice when the surface energy anisotropy of the solid-liquid and solid-solid phase boundaries is small enough to prevent locking of the lamellae to preferred growth directions. When used to analyze heuristically the long-wavelength stability of a eutectic front, this hypothesis leads to the conclusion that the lamellar structure is unstable for lamellar spacings below $\lambda_{\min}$. Under Cahn's hypothesis, the lamellar spacing in a concave part of the solid-liquid interface decreases as the interface advances. Consequently, if the average spacing falls below $\lambda_{\min}$, the local undercooling will increase in such a way that thinner lamellae fall further behind the front, leading finally to lamella termination. On the other hand, for spacings larger than $\lambda_{\min}$, the opposite occurs: finer lamellae grow faster than wider ones and the concavity of the eutectic front is smoothed out.

This argument can determine only a lower bound for λ. To assess stability for $\lambda > \lambda_{\min}$, a more involved analysis is required. Several authors tried to adapt the linear stability analysis of Mullins and Sekerka for single-phase solidification [10] to eutectic systems. The eutectic problem, however, is considerably more difficult because the basic steady-state solution is already periodic in space. Moreover, the presence of *mobile* trijunction points between three phases complicates enormously the stability calculation by ruling out a smooth sinusoidal perturbation. For this reason, early attempts to average over the properties of the two solid phases [17], or to consider perturbations with immobile trijunctions [18–20], did not produce consistent results (see Ref. [21] for a more detailed discussion).

The most complete analytical stability analysis of a eutectic interface has been performed by Datye and Langer (DL) [22]. Their calculation is a perturbation analysis of the Jackson-Hunt (JH) [15] steady-state solution, using as basic variables the coordinates of the trijunction points both parallel and perpendicular to the interface. They first calculate an approximate solution to the diffusion equation for a perturbed lamellar interface. The assumption of local equilibrium at the solid-liquid interface and the use of Cahn's hypothesis then allow one to obtain an eigenvalue problem for the linear growth modes and to extract the stability spectrum of the interface. In the limit where the wavelength of the perturbation is large compared to the lamellar spacing (referred to hereafter as the ''long-wavelength limit''), a simplified calculation confirms JH's conclusion that lamellar spacings below $\lambda_{\min}$ are unstable [23]. In addition, the DL analysis predicted the occurrence of an oscillatory instability with a wavelength twice the lamellar spacing for sufficiently off-eutectic compositions (2λ-O instability).

The existence of this short-wavelength instability was later confirmed by numerical simulations of eutectic front dynamics using a random walk algorithm [24] and, more recently, a boundary integral approach [21,25]. The latter study pinpointed the existence of additional short-

wavelength instabilities, one of which (tilt bifurcation) was previously known [24,26], and made specific quantitative predictions for the CBr_4-C_2Cl_6 organic system that have been validated by a detailed comparison with experiments [27,28]. As an additional result, which is relevant for the present analysis, the boundary integral study revealed that the stability predictions of the DL analysis are quite accurate for lamellar spacings close to λ_{min}, and only become inaccurate for larger spacings where the JH description of the diffusion field breaks down.

In summary, according to both theory and experiment, a planar lamellar eutectic front in a binary alloy is completely stable for compositions sufficiently close to the eutectic composition, and for lamellar spacings near λ_{min}. To understand the instability leading to colony formation, one must therefore include a ternary impurity. To date, few theoretical studies of ternary systems have been available. Rinaldi, Sharp, and Flemings derived a generalized constitutional supercooling criterion for ternary systems and used it to interpret their experiments [9]. McCartney, Hunt, and Jordan adapted the JH steady-state analysis to include impurities. They interpreted the formation of colonies as the result of a Mullins-Sekerka instability driven by the ternary impurity [29], but did not carry out a detailed stability analysis.

In this paper, we extend Datye and Langer's linear stability approach, based on a Jackson-Hunt approximation of the diffusion field, to include the effect of a ternary impurity. For the reasons mentioned above, we expect this approach to yield relatively accurate predictions for spacings close to λ_{min}, which is typically the dynamically selected range of interest in experiments. We obtain the full linear stability spectrum of the steady-state lamellar eutectic front growing in two dimensions. Our final result is quite complicated, but can be substantially simplified for a model alloy with a symmetric phase diagram, solidified at its eutectic composition. From the study of this special case, we can identify all important factors that determine the stability of the front. In particular, we find that the interlamellar eutectic diffusion field gives a stabilizing contribution with a functional form similar to the usual capillary term. Thus, this contribution leads effectively to a ''renormalization'' of the capillary length. Using this insight, we are able to reformulate the stability problem by treating the large scale dynamics of the eutectic front as an ''effective monophase interface,'' as suggested by Fig. 1, with a Gibbs-Thomson condition that is coupled to an equation of motion for the local lamellar spacing. A similar type of approach has been used previously to analyze the long-wavelength modes of cellular arrays during directional solidification of dilute binary alloys [30]. More recent numerical work, however, has shown that the modes that limit the range of stable cell spacings at low velocity are oscillatory and nonoscillatory instabilities with a wavelength equal to twice the cell spacing [31] that have been observed in experiments [32]. In contrast, here, no short-wavelength instabilities are present near the eutectic composition for λ close to λ_{min}. Therefore, the effective interface approach provides an accurate description of the interface dynamics in the limit of perturbation wavelengths much larger than the lamellar spacing. Moreover, it can be extended to derive a simplified expression for the stability spectrum by incorporating phenomenologically the effect of surface tension. This formula is found to predict all important features of the instability and to yield reasonably good quantitative predictions.

Our calculation both confirms the expectations based on the analogy between a two-phase eutectic front in the presence of a ternary impurity and a monophase front, and at the same time yields a surprising result. Namely, we find that the expressions for the onset velocity and wavelength of the instability are analogous to those for a monophase front with a surface tension renormalized by the geometry of the lamellar front and interlamellar diffusion. Thus, as far as these quantities are concerned, the lamellar structure leads to quantitative differences, but no new qualitative features of the instability. The new ingredient, however, which could not have been expected on the basis of the analogy with a monophase front, is that the instability is oscillatory. The origin of this difference is due to the additional degrees of freedom associated with the underlying lamellar structure of the interface. According to Cahn's hypothesis, the change in the local lamellar spacing is determined by the shape of the front. The spacing, in turn, is related to the local interface temperature. As a consequence of the interplay between this effect and the instability driven by the impurities, long-wavelength perturbations may oscillate during growth or form traveling waves. There indeed seems to be recent experimental evidence for such large scale oscillatory behavior near the onset of colony formation in a transparent organic model alloy [33].

We also investigate the influence of the ternary impurity on the short-wavelength (2λ-O) oscillatory instability that is already present in a binary eutectic. The main result is that this instability is enhanced by the impurity boundary layer, which leads to a reduced composition range for stable lamellar growth even below constitutional supercooling.

The structure of this paper is as follows. In Sec. II, we introduce the basic sharp-interface equations. We then summarize in Sec. III the Jackson-Hunt approach and apply it to calculate the steady-state solution in the presence of a ternary impurity. In Sec. IV, we review the principles of the DL approach and calculate the additional terms arising from the presence of an impurity. Section V is devoted to a detailed discussion of the stability spectrum at the eutectic composition in a model phase diagram that is symmetric about this composition. In Sec. VI, we reformulate the stability problem in terms of an effective interface approach and derive an approximate expression for the stability spectrum for an arbitrary phase diagram and material parameters. In Sec. VII, we discuss how the off-eutectic short-wavelength oscillatory instability is affected by the ternary impurity. Finally, we summarize our main results in Sec. VIII.

II. BASIC EQUATIONS

We study the solidification of a binary eutectic alloy containing a small amount of ternary impurity. Let c denote the concentration (in molecules per unit volume) of one of the constituents of the binary eutectic, and $\tilde{c}$ the concentration of the ternary impurity. As we restrict our attention to small impurity concentrations, we shall assume that these two quantities can be treated as independent variables. In other words, we assume that the phase diagram of the binary eutectic is only slightly altered by the presence of the impurity.

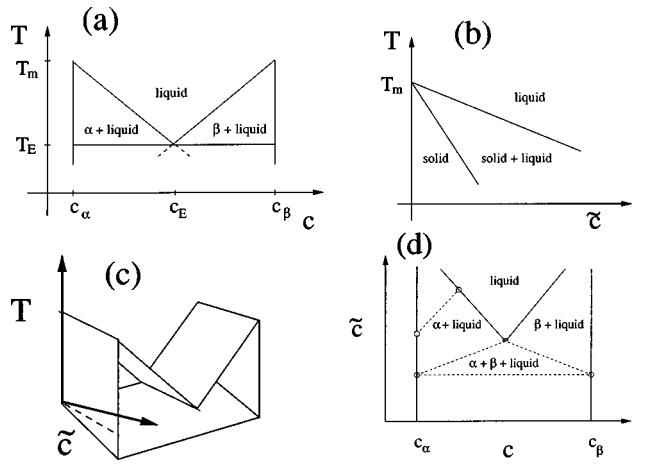

FIG. 2. Phase diagram of an idealized ternary eutectic alloy. (a) Binary eutectic phase diagram ($\tilde{c}=0$). T_m is the melting temperature of the pure phases, T_E the eutectic temperature, and c_E the eutectic composition. (b) Cut through the ternary diagram along the eutectic valley ($c=c_E$). (c) Liquidus and solidus surfaces in the space $(c,\tilde{c},T)$. The dashed line is the projection of the eutectic valley on the solidus surface. The liquidus surfaces have metastable extensions beyond the eutectic valley (not shown). (d) Coexistence curves for a fixed temperature below T_E in the $(c,\tilde{c})$ plane.

The two solid phases are denoted by α and β; c_α and c_β are the concentrations limiting the eutectic plateau in the binary phase diagram, $\Delta c=c_\beta-c_\alpha$, and c_E is the eutectic composition.

For coupled eutectic growth, the temperature of the lamellar front is close to the eutectic temperature, and the composition on the liquid side of the solid-liquid interface is close to the eutectic point [15]. This allows us to introduce two further simplifications. First, we may approximate the solidus and liquidus surfaces in the ternary phase diagram by planes around the eutectic point. We denote by m_s and $\tilde{m}_s$ $(s=\alpha,\beta)$ the magnitude of the liquidus slopes along the c- and $\tilde{c}$-axis, respectively. Second, we will assume that c_α and c_β are independent of temperature and impurity concentration. As already argued by DL, this should only slightly affect the final results, because in the temperature range explored by the front the relative variations of the concentration jumps across the interfaces are negligible. On the other hand, our calculations are considerably simplified, as we can relate the volume fraction η of the α solid to the composition of the melt far ahead of the interface, c_∞, via the relation

$$c_\infty=c_\alpha\eta+c_\beta(1-\eta), \tag{1}$$

independently of the concentration of the ternary impurity and the interface temperature. For the impurity, we will work in a dilute alloy approximation where the impurity concentrations on the solid and liquid sides of the interface are related in equilibrium by

$$\tilde{c}_s=\tilde{k}_s\tilde{c}_L, \quad s=\alpha,\beta. \tag{2}$$

The resulting phase diagram in the space $(c,\tilde{c},T)$ is sketched in Fig. 2. The line of intersection of the two liquidus surfaces is usually termed the *eutectic valley* or *eutectic trough*. Along this line, c, $\tilde{c}$, and T are related by the equations

$$c-c_E=\frac{\tilde{m}_\beta-\tilde{m}_\alpha}{m_\alpha+m_\beta}\tilde{c}, \tag{3}$$

$$T-T_E=\tilde{M}\tilde{c}, \tag{4}$$

$$\tilde{M}=\frac{\tilde{m}_\alpha m_\beta+m_\alpha\tilde{m}_\beta}{m_\alpha+m_\beta}. \tag{5}$$

Equation (3) defines a monovariant line in the ternary phase diagram where, except for the special case $\tilde{m}_\alpha=\tilde{m}_\beta$, the eutectic composition is shifted with respect to the binary eutectic point in the presence of a ternary impurity. $\tilde{M}$ is the liquidus slope along the eutectic valley. A liquid satisfying Eqs. (3) and (4) can be in simultaneous equilibrium with two solids.

In a typical directional solidification experiment, the sample is pulled in a temperature gradient G with a constant pulling speed v_p. We assume that heat diffusion is much faster than chemical diffusion and that the thermal conductivities of solid and liquid are of comparable magnitude. Under this set of assumptions (commonly referred to as the frozen temperature approximation), the temperature is given by

$$T(z)=T_E+Gz, \tag{6}$$

where we have chosen the origin of the z axis at the eutectic temperature.

In the absence of convection, the growth of the solid is limited by chemical diffusion of the constituents. We assume zero diffusivity in the solid (one-sided model). In the liquid, the diffusion equations in the laboratory frame (moving with velocity v_p with respect to the sample) are

$$\frac{1}{D}\frac{\partial c}{\partial t}=\frac{2}{l}\partial_z c+\vec{\nabla}^2 c, \tag{7a}$$

$$\frac{1}{\tilde{D}}\frac{\partial \tilde{c}}{\partial t}=\frac{2}{\tilde{l}}\partial_z \tilde{c}+\vec{\nabla}^2 \tilde{c}, \tag{7b}$$

with the diffusion lengths $l=2D/v_p$ and $\tilde{l}=2\tilde{D}/v_p$, D and $\tilde{D}$ being the diffusivities of the eutectic components and the ternary impurity, respectively.

For lamellar eutectic growth in thin-film geometry, the problem is essentially two-dimensional. Let the position of the solid-liquid interface be described by the curve $\zeta(x,t)$. During the phase transformation, impurities and the minor component of the growing solid are rejected into the liquid. The condition of mass conservation implies that at the interface

$$-D\partial_n c=v_n[c(x,\zeta)-c_\alpha] \quad (\alpha\text{L-interface}), \tag{8a}$$

$$-D\partial_n c=v_n[c(x,\zeta)-c_\beta] \quad (\beta\text{L-interface}), \tag{8b}$$

$$-\tilde{D}\partial_n \tilde{c}=v_n(1-\tilde{k}_\alpha)\tilde{c}(x,\zeta) \quad (\alpha\text{L-interface}), \tag{8c}$$

$$-\tilde{D}\partial_n \tilde{c}=v_n(1-\tilde{k}_\beta)\tilde{c}(x,\zeta) \quad (\beta\text{L-interface}), \tag{8d}$$

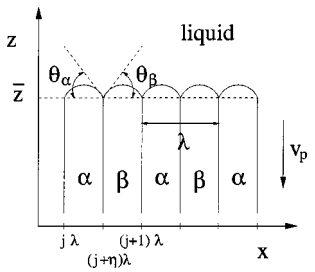

FIG. 3. Sketch of a steady-state array of lamellae growing parallel to the z axis. The lamella pairs are numbered by the integer j, η is the volume fraction of α-phase, and $\bar{z}$ is the z coordinate of the trijunction points.

where v_n and ∂_n denote the normal velocity of the interface and the derivative normal to the interface, respectively.

We are interested in a regime of relatively low solidification velocity where the solid-liquid interface can be considered to be in local equilibrium, in which case the temperature and concentration fields at the interface are related by the Gibbs-Thomson conditions

$$T = T_E - m_\alpha(c_L - c_E) - \tilde{m}_\alpha \tilde{c}_L - \Gamma_\alpha K[\zeta] \quad (\alpha L\text{-interface}), \tag{9a}$$

$$T = T_E + m_\beta(c_L - c_E) - \tilde{m}_\beta \tilde{c}_L - \Gamma_\beta K[\zeta] \quad (\beta L\text{-interface}). \tag{9b}$$

Here, $K[\zeta]$ is the local interface curvature, and

$$\Gamma_s = T_E \gamma_{sL}/L_s, \quad s = \alpha, \beta, \tag{10}$$

are the Gibbs-Thomson constants, with γ_{sL} and L_s denoting, respectively, the liquid-solid surface tensions and the latent heats of the two solids at the eutectic point.

Finally, local equilibrium also implies that at the trijunction points, where the three phases are in contact, the angles between the three interfaces are fixed by the balance of surface tension forces, which for isotropic interfaces yields the two conditions

$$\gamma_{\alpha L} \sin\theta_\alpha + \gamma_{\beta L} \sin\theta_\beta = \gamma_{\alpha\beta}, \tag{11a}$$

$$\gamma_{\alpha L} \cos\theta_\alpha = \gamma_{\beta L} \cos\theta_\beta, \tag{11b}$$

where the definition of the angles θ_α and θ_β is illustrated in Fig. 3.

III. STEADY-STATE SOLUTION

For a binary eutectic, the steady-state problem has been treated by Jackson and Hunt [15]. Their method has been extended to ternary systems by McCartney, Hunt, and Jordan [29]. We need the steady-state solution as the starting point for our stability analysis. We will only summarize here the essential steps of the calculation; more details can be found in Refs. [15,22,29].

A typical configuration for a lamellar eutectic growing at constant solidification speed v_p is sketched in Fig. 3. Alternating lamellae of the α and β phase are regularly spaced. The width of one lamella pair, λ, is usually of the order of 10 μm. We must find the interface shape for which the diffusion equations and the Gibbs-Thomson conditions at the interface are both satisfied. The JH approximation starts by solving the diffusion problem for a flat interface (consisting of lamellae with $\theta_\alpha = \theta_\beta = 0$). This can be achieved by expanding the diffusion field in Fourier modes along the x axis:

$$c(x,z) = c_\infty + \sum_{n=-\infty}^{\infty} B_n \exp[iq_n x - \bar{q}_n(z - \bar{z})], \tag{12}$$

with $q_n = 2\pi n/\lambda$, and $\bar{z}$ the z coordinate of the trijunction points. The constants $\bar{q}_n$ are obtained by substituting the above sum into the diffusion equation. Since time derivatives are zero in steady state, this yields, at once,

$$\bar{q}_n = 1/l + \sqrt{1/l^2 + q_n^2}. \tag{13}$$

Inserting the expansion (12) into the mass conservation condition allows us to determine all Fourier coefficients except for B_0. The average undercooling for each lamella can then be calculated using the Gibbs-Thomson conditions. Finally, the condition that the two phases must grow at equal undercooling determines B_0 and the average undercooling ΔT of the solid-liquid interface as a function of λ and η.

For a eutectic with a ternary impurity, we must in addition treat the diffusion of the ternary impurity in the liquid phase. For this purpose, we use the same Fourier expansion as above,

$$\tilde{c}(x,z) = \tilde{c}_\infty + \sum_{n=-\infty}^{\infty} \tilde{B}_n \exp[iq_n x - \tilde{q}_n(z - \bar{z})], \tag{14}$$

where $\tilde{c}_\infty$ is the impurity concentration far from the interface, and the constants $\tilde{q}_n$ are equivalent to $\bar{q}_n$ with l replaced by $\tilde{l}$. This expansion is inserted into the condition for impurity conservation at the interface. To extract an equation for the Fourier coefficients $\tilde{B}_n$, both sides of the equation are then multiplied by $\exp(-iq_m x)$ and integrated over x from 0 to λ. The result for the coefficient $\tilde{B}_0$, which gives the magnitude of the overall diffusion boundary layer, can be written in the form

$$\tilde{B}_0 = \tilde{c}_\infty \left(\frac{1}{k_E} - 1 \right), \tag{15}$$

with an effective partition coefficient

$$k_E = \eta \tilde{k}_\alpha + (1 - \eta)\tilde{k}_\beta. \tag{16}$$

For $n \neq 0$, we obtain

$$\tilde{q}_n \tilde{B}_n = \frac{2}{\tilde{l}} \left(1 - \frac{\tilde{k}_\alpha + \tilde{k}_\beta}{2} \right) \tilde{B}_n + \frac{2}{\tilde{l}} (\tilde{k}_\beta - \tilde{k}_\alpha) \left\{ \tilde{c}_\infty \frac{e^{-iq_n \eta\lambda} - 1}{-i\lambda q_n} + (\eta - \tfrac{1}{2})\tilde{B}_n + \sum_{m \neq n} \frac{e^{i(q_n - q_m)\eta\lambda} - 1}{i\lambda(q_n - q_m)} \tilde{B}_m \right\}. \tag{17}$$

We are interested in a growth regime where the diffusion length is much larger that the lamellar spacing, and the Péclet number, $\mathrm{Pe} = \lambda/l \ll 1$. Consequently, for $n \neq 0$, we have

$\tilde{q}_n \gg 1/\tilde{l}$, and all terms containing the coefficients $\tilde{B}_n$ on the right-hand side (RHS) of Eq. (17) can be neglected, which yields

$$\tilde{B}_n = \frac{4\tilde{c}_\infty(\tilde{k}_\beta - \tilde{k}_\alpha)e^{-iq_n\eta\lambda/2}\sin(q_n\eta\lambda/2)}{\lambda q_n \tilde{q}_n \tilde{l}}. \tag{18}$$

Note that, if we want to go beyond this approximation, the problem becomes considerably more involved, because then all the Fourier coefficients are coupled.

We proceed now as JH by calculating the average impurity concentration in front of each phase, that is, by evaluating

$$\langle \tilde{c} \rangle_\alpha = \frac{1}{\eta\lambda}\int_0^{\eta\lambda} \tilde{c}(x,z)dx, \tag{19a}$$

$$\langle \tilde{c} \rangle_\beta = \frac{1}{(1-\eta)\lambda}\int_{\eta\lambda}^{\lambda} \tilde{c}(x,z)dx \tag{19b}$$

at $z=\overline{z}$. The results are

$$\langle \tilde{c} \rangle_\alpha = \frac{\tilde{c}_\infty}{k_E} + \frac{2\lambda}{\tilde{l}\eta}P(\eta)\tilde{c}_\infty(\tilde{k}_\beta - \tilde{k}_\alpha), \tag{20a}$$

$$\langle \tilde{c} \rangle_\beta = \frac{\tilde{c}_\infty}{k_E} - \frac{2\lambda}{\tilde{l}(1-\eta)}P(\eta)\tilde{c}_\infty(\tilde{k}_\beta - \tilde{k}_\alpha), \tag{20b}$$

with

$$P(\eta) = \sum_{n=1}^{\infty} \frac{1}{(\pi n)^3}\sin^2(\pi\eta n). \tag{21}$$

Averaging the Gibbs-Thomson condition over individual lamellae, we obtain the mean undercooling of the solid-liquid interface:

$$\langle \Delta T \rangle_\alpha = m_\alpha(\langle c \rangle_\alpha - c_E) + \tilde{m}_\alpha \langle \tilde{c} \rangle_\alpha + \Gamma_\alpha \langle K \rangle_\alpha, \tag{22a}$$

$$\langle \Delta T \rangle_\beta = -m_\beta(\langle c \rangle_\beta - c_E) + \tilde{m}_\beta \langle \tilde{c} \rangle_\beta + \Gamma_\beta \langle K \rangle_\beta, \tag{22b}$$

where the average values $\langle \Delta T \rangle_s$, $\langle c \rangle_s$, and $\langle K \rangle_s$ $(s=\alpha,\beta)$ are defined by expressions analogous to Eqs. (19) for $\langle \tilde{c} \rangle_s$. The averages for the composition, $\langle c \rangle_s$, and for the curvatures, $\langle K \rangle_s$, are [22]

$$\langle c \rangle_\alpha - c_E = c_\infty + B_0 + \frac{2\lambda\Delta c}{l\eta}P(\eta), \tag{23a}$$

$$\langle c \rangle_\beta - c_E = c_\infty + B_0 - \frac{2\lambda\Delta c}{l(1-\eta)}P(\eta), \tag{23b}$$

$$\langle K \rangle_\alpha = \frac{2}{\eta\lambda}\sin\theta_\alpha, \tag{24a}$$

$$\langle K \rangle_\beta = \frac{2}{(1-\eta)\lambda}\sin\theta_\beta. \tag{24b}$$

The last step is to apply the condition that neighboring lamellae should grow at equal undercooling, $\langle \Delta T \rangle_\alpha = \langle \Delta T \rangle_\beta$. This determines the only degree of freedom left in the problem: the eutectic boundary layer B_0. The solution is

$$B_0 = -(c_\infty - c_E) + \frac{\tilde{c}_\infty}{k_E}\frac{\tilde{m}_\beta - \tilde{m}_\alpha}{m_\alpha + m_\beta} + \frac{2\lambda P(\eta)\Delta c}{m_\alpha + m_\beta} \times \left[\frac{1}{l}\left(\frac{m_\beta}{1-\eta} - \frac{m_\alpha}{\eta}\right) - \frac{1}{\tilde{l}}\left(\frac{\tilde{m}_\alpha}{\eta} + \frac{\tilde{m}_\beta}{1-\eta}\right)\frac{\tilde{c}_\infty}{\Delta c}(\tilde{k}_\beta - \tilde{k}_\alpha)\right]. \tag{25}$$

There are two terms that are not present in the binary eutectic. The second term on the RHS of Eq. (25) gives, according to Eq. (3), the shift of the eutectic composition corresponding to an impurity concentration $\tilde{c}_\infty/k_E$. It is remarkable that, even for a system that started from an initial state with three-phase equilibrium, a eutectic boundary layer must develop in order that the composition condition for three-phase equilibrium at the trijunction points can be met. The second new term is the last term in brackets on the RHS of Eq. (25), involving the difference of the partition coefficients. This term is due to the unequal rejection of impurities in the liquid.

The interfacial undercooling as a function of the lamellar spacing can be written in a form very similar to the JH result for a simple binary eutectic:

$$\Delta T = \tilde{M}\frac{\tilde{c}_\infty}{k_E} + \frac{1}{2}\Delta T_{\min}\left(\frac{\lambda}{\lambda_{\min}} + \frac{\lambda_{\min}}{\lambda}\right). \tag{26}$$

The first term, according to Eq. (4), gives the undercooling of the point in the eutectic valley corresponding to an impurity concentration $\tilde{c}_\infty/k_E$. The minimum undercooling $\Delta T_{\min}$ and the corresponding spacing $\lambda_{\min}$ are

$$\Delta T_{\min} = \frac{4\Delta c}{\eta(1-\eta)}\left(\frac{m_\alpha m_\beta}{m_\alpha + m_\beta}\right)\sqrt{f(\eta)p(\eta,\tilde{c}_\infty)}, \tag{27}$$

$$\lambda_{\min} = \sqrt{f(\eta)/p(\eta,\tilde{c}_\infty)}, \tag{28}$$

with

$$f(\eta) = \frac{(1-\eta)\Gamma_\alpha\sin\theta_\alpha}{m_\alpha\Delta c} + \frac{\eta\Gamma_\beta\sin\theta_\beta}{m_\beta\Delta c}, \tag{29}$$

$$p(\eta,\tilde{c}_\infty) = \frac{P(\eta)}{l} + \frac{P(\eta)}{\tilde{l}}\frac{\tilde{c}_\infty}{\Delta c}(\tilde{k}_\beta - \tilde{k}_\alpha) \times \left[(1-\eta)\frac{\tilde{m}_\alpha}{m_\alpha} - \eta\frac{\tilde{m}_\beta}{m_\beta}\right]. \tag{30}$$

Note that, as in a binary eutectic, we have $\Delta T_{\min} \sim \sqrt{v_p}$ and $\lambda_{\min} \sim 1/\sqrt{v_p}$. In the special case $\tilde{k}_\alpha = \tilde{k}_\beta$, we recover the classic JH result. The two λ-dependent terms on the RHS of Eq. (26) represent the effects of diffusion and surface tension. For finer lamellae, the diffusion between adjacent lamellae is faster, and the undercooling due to the concentration term in the Gibbs-Thomson relation is smaller. This

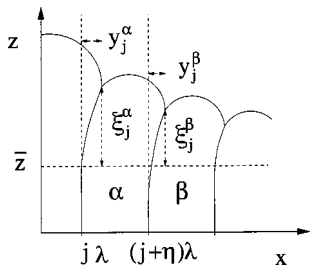

FIG. 4. Sketch of a perturbed lamellar interface, showing the displacements y_j^α, y_j^β, ξ_j^α, and ξ_j^β.

gives the term proportional to λ. On the other hand, for finer lamellae the average curvature is higher due to the constraints at the trijunction points, leading to the term proportional to λ^{-1}.

For our subsequent stability analysis, we will now simplify the problem. The main effect of the impurities, rejected by both solid phases, is the buildup of the impurity boundary layer of amplitude $\tilde{B}_0$. The diffusion of impurities between neighboring lamellae leads to corrections in $\lambda_{\min}$ and $\Delta T_{\min}$. In the dilute limit, however, where $\tilde{c}_\infty \ll \Delta c$, these corrections are small. In addition, the partition coefficients for ternary impurities are often close to zero, and we have $\tilde{k}_\alpha - \tilde{k}_\beta \ll 1$. Thus it seems well justified to make the approximation $p(\eta, \tilde{c}_\infty) \approx P(\eta)/l$ in Eq. (30) and to drop the term involving the difference of the partition coefficients in Eq. (25). This means that we neglect the interlamellar impurity diffusion modes, $\tilde{B}_n = 0$ for $n \neq 0$, which is equivalent to the assumption of equal impurity partition coefficients, $\tilde{k}_\alpha = \tilde{k}_\beta = k_E$. For two very different impurity partition coefficients, it might be necessary to go beyond this approximation and to include the interlamellar impurity diffusion.

We will also assume equal impurity liquidus slopes $\tilde{m}_\alpha$ and $\tilde{m}_\beta$ for most of what follows. Then, the eutectic composition and the magnitude of the eutectic boundary layer, described by the coefficient B_0, do not depend on the impurity concentration. We will briefly comment on the general case at the end of Sec. VI.

IV. STABILITY ANALYSIS

The DL method is a perturbation analysis around the JH steady-state solution. The fundamental variables in this approach are the coordinates of the trijunction points, or more precisely, the departure of these coordinates from their steady-state values. As illustrated in Fig. 4, the coordinates of the trijunction points of the jth lamella pair are written as

$$x_j^\alpha = j\lambda + y_j^\alpha(t) \quad x_j^\beta = (j+\eta)\lambda + y_j^\beta(t), \tag{31}$$

$$z_j^\alpha = \bar{z} + \xi_j^\alpha(t) \quad z_j^\beta = \bar{z} + \xi_j^\beta(t). \tag{32}$$

We assume the system to consist of a total number of N lamella pairs, and use periodic boundary conditions. For convenience, we define a dimensionless eutectic concentration field by

$$u = \frac{c - c_E}{\Delta c}, \tag{33}$$

and a dimensionless impurity concentration field

$$\tilde{u} = \frac{\tilde{c} - \tilde{c}_\infty}{\Delta \tilde{c}}, \tag{34}$$

with $\Delta \tilde{c} = \tilde{c}_\infty (1/k_E - 1)$.

Let us outline the strategy of the DL calculation. For a slowly evolving, slightly perturbed interface, the Gibbs-Thomson condition for local equilibrium remains satisfied. The deformation of the front modifies the local curvatures and concentrations. The perturbed diffusion fields can be calculated using the mass conservation conditions. For small displacements, all resulting expressions are linearized in ξ_j^s and y_j^s. To close the set of equations, DL use Cahn's hypothesis, which gives additional relations between the ξ's and the y's. Inserting all these expressions into the Gibbs-Thomson condition allows one to determine the stability spectrum of the interface.

The new element here is the ternary impurity diffusion field. To obtain the modifications it generates in the stability spectrum, we have to introduce the procedure in more detail. As in the JH calculation, a complete solution of the free boundary problem is out of reach, and we use quantities that are averaged over individual lamellae. The average undercooling of a lamella is written as

$$\Delta T_j^s(t) = \Delta T + \delta T_j^s(t) \quad (s = \alpha, \beta), \tag{35}$$

with ΔT, the steady-state value, given by Eq. (26). To express the $\delta T_j^s(t)$'s, we have to calculate the deviations of curvature and concentrations from their steady-state values; that is,

$$\delta\langle K\rangle_j^\alpha(t) = \frac{1}{x_j^\beta - x_j^\alpha}\int_{x_j^\alpha}^{x_j^\beta} K[\zeta(x,t)]\,dx - \langle K\rangle_\alpha, \tag{36a}$$

$$\delta\langle K\rangle_j^\beta(t) = \frac{1}{x_{j+1}^\alpha - x_j^\beta}\int_{x_j^\beta}^{x_{j+1}^\alpha} K[\zeta(x,t)]\,dx - \langle K\rangle_\beta, \tag{36b}$$

$$\delta\langle u\rangle_j^\alpha(t) = \frac{1}{x_j^\beta - x_j^\alpha}\int_{x_j^\alpha}^{x_j^\beta} u(x,\zeta(x,t),t)\,dx - \langle u\rangle_\alpha, \tag{37a}$$

$$\delta\langle u\rangle_j^\beta(t) = \frac{1}{x_{j+1}^\alpha - x_j^\beta}\int_{x_j^\beta}^{x_{j+1}^\alpha} u(x,\zeta(x,t),t)\,dx - \langle u\rangle_\beta, \tag{37b}$$

with the equivalent quantities for the ternary impurity field being obtained by replacing u by $\tilde{u}$ in the last two equations above. The steady-state values are obtained from Eqs. (20) and (23) using the changes of variables (33) and (34). Furthermore, we define the average z position of a lamella by

$$\langle \xi \rangle_j^{\alpha} = \frac{1}{2}(\xi_j^{\alpha} + \xi_j^{\beta}), \tag{38a}$$

$$\langle \xi \rangle_j^{\beta} = \frac{1}{2}(\xi_{j+1}^{\alpha} + \xi_j^{\beta}). \tag{38b}$$

In terms of these local averages, the linearized Gibbs-Thomson conditions read

$$\delta T_j^{\alpha}(t) = -G\langle \xi \rangle_j^{\alpha}(t) = m_{\alpha}\delta\langle u \rangle_j^{\alpha}(t) + \tilde{m}_{\alpha}\delta\langle \tilde{u} \rangle_j^{\alpha}(t) + \Gamma_{\alpha}\delta\langle K \rangle_j^{\alpha}(t), \tag{39a}$$

$$\delta T_j^{\beta}(t) = -G\langle \xi \rangle_j^{\beta}(t) = -m_{\beta}\delta\langle u \rangle_j^{\beta}(t) + \tilde{m}_{\beta}\delta\langle \tilde{u} \rangle_j^{\beta}(t) + \Gamma_{\beta}\delta\langle K \rangle_j^{\beta}(t). \tag{39b}$$

The next step is to express the averages in the two equations above in terms of the displacements ξ_j^s and y_j^s. For the curvature terms, the procedure is straightforward, but for the diffusion fields one needs to introduce a piecewise linear representation of the interface shape, as will be described in more detail below [see Eq. (52)]. Following this step, Eqs. (39) become a system of $2N$ linear equations for $4N$ variables and their time derivatives. To complete this system, we must specify how the trijunction points react to deformations of the growth front. Following DL, we will use Cahn's hypothesis and assume that the trijunctions always grow perpendicular to the eutectic solidification front, which yields the conditions

$$\dot{y}_j^{\alpha} = -(\xi_j^{\beta} - \xi_{j-1}^{\beta})v_p/\lambda, \tag{40a}$$

$$\dot{y}_j^{\beta} = -(\xi_{j+1}^{\alpha} - \xi_j^{\alpha})v_p/\lambda, \tag{40b}$$

where the dot denotes the time derivative.

We now transform the problem into an eigenvalue equation by analyzing it in terms of time-dependent Fourier modes. We write

$$\xi_j^s = X_k^s \exp(ik\lambda j + \omega t) \quad (s = \alpha, \beta), \tag{41a}$$

$$y_j^s = Y_k^s \exp(ik\lambda j + \omega t) \quad (s = \alpha, \beta), \tag{41b}$$

where the allowed wave vectors k are integer multiples of $2\pi/N\lambda$ and lie in the interval $[-\pi/\lambda, \pi/\lambda]$. In the limit of an infinite number of lamellae, $N \to \infty$, we recover a continuous spectrum. The growth constraints (40) give then immediately

$$\omega Y_k^{\alpha} = -\frac{2iv_p}{\lambda} e^{-ik\lambda/2} \sin(k\lambda/2) X_k^{\beta}, \tag{42a}$$

$$\omega Y_k^{\beta} = -\frac{2iv_p}{\lambda} e^{ik\lambda/2} \sin(k\lambda/2) X_k^{\alpha}. \tag{42b}$$

This allows us to eliminate the coefficients Y_k^{α} and Y_k^{β}, and the only unknowns left in the problem are X_k^{α}, X_k^{β}, and ω. It is useful to write each of the terms appearing in the Gibbs-Thomson condition in the compact forms

$$G\langle \xi \rangle_j^s(t) = e^{ik\lambda j + \omega t} \sum_{s' = \alpha, \beta} \mathbf{G}^{s,s'}(k, \omega) X_k^{s'}, \tag{43}$$

$$\delta\langle K \rangle_j^s(t) = e^{ik\lambda j + \omega t} \sum_{s' = \alpha, \beta} \mathbf{K}^{s,s'}(k, \omega) X_k^{s'}, \tag{44}$$

$$\delta\langle u \rangle_j^s(t) = e^{ik\lambda j + \omega t} \sum_{s' = \alpha, \beta} \mathbf{U}^{s,s'}(k, \omega) X_k^{s'}, \tag{45}$$

$$\delta\langle \tilde{u} \rangle_j^s(t) = e^{ik\lambda j + \omega t} \sum_{s' = \alpha, \beta} \tilde{\mathbf{U}}^{s,s'}(k, \omega) X_k^{s'}. \tag{46}$$

Then, the conditions (39) can be written as an eigenvalue equation,

$$\sum_{s' = \alpha, \beta} \mathbf{A}^{s,s'} X_k^{s'} = 0, \tag{47}$$

where the matrix $\mathbf{A}$ is given by

$$\mathbf{A} = \mathbf{G} + \begin{pmatrix} \Gamma_{\alpha} & 0 \\ 0 & \Gamma_{\beta} \end{pmatrix} \mathbf{K} + \begin{pmatrix} m_{\alpha}\Delta c & 0 \\ 0 & -m_{\beta}\Delta c \end{pmatrix} \mathbf{U} + \begin{pmatrix} \tilde{m}_{\alpha}\Delta\tilde{c} & 0 \\ 0 & \tilde{m}_{\beta}\Delta\tilde{c} \end{pmatrix} \tilde{\mathbf{U}}. \tag{48}$$

The first three terms on the RHS of Eq. (48) are identical to those calculated by DL, whereas the last term is due to the presence of the ternary impurity. For a given wave number k, Eq. (47) is fulfilled only for special values of ω. The solvability condition,

$$\det \mathbf{A} = 0, \tag{49}$$

gives the dispersion relations $\omega(k)$.

The core of the problem is the calculation of the matrices appearing in Eq. (48). The first two, $\mathbf{G}$ and $\mathbf{K}$, are relatively easy (see Ref. [22] and Appendix A). The most difficult is the matrix $\mathbf{U}$. We start by writing the perturbed diffusion field as

$$u(x,z,t) = u_0(x,z) + \delta u(x,z,t), \tag{50}$$

where $u_0(x,z)$ is the steady-state solution. Next, δu is expanded in Fourier modes; this time with the periodicity of the whole system, i.e., with wave numbers $p = 2\pi n/N\lambda$:

$$\delta u(x,z,t) = \sum_p b_p \exp[ipx - \overline{q}_p(z - \overline{z}) + \omega t]. \tag{51}$$

The p's, unlike the k's, range from $-\infty$ to ∞, because the diffusion field is continuous. To simplify our calculations, we use the quasistationary approximation for the diffusion equation; i.e., we drop the time derivative in Eq. (7a). Physically, this means that we assume that the diffusion field adjusts instantaneously to any change in the interface configuration. For a perturbation such as that given by Eq. (51), this is justified if $|\omega| \ll Dp^2$ and $|\omega| \ll Dp/l$, conditions that will be checked *a posteriori* at the end of Sec. V D. In the range of wavelength of interest here, i.e. for $\lambda < 2\pi/p < l$, we find

that these conditions are generally well satisfied. Within this approximation, the constants $\overline{q_p}$ are given by the analog of Eq. (13).

To obtain the Fourier coefficients b_p, we proceed as in the steady-state calculation and insert the expansion in the mass conservation condition. To make the problem tractable, the actual interface shape $\zeta(x,t)$ is replaced by the piecewise constant function

$$\zeta(x,t)-\overline{z}=\begin{cases}\langle\xi\rangle_j^\alpha, & x_j^\alpha<x<x_j^\beta,\\ \langle\xi\rangle_j^\beta, & x_j^\beta<x<x_{j+1}^\alpha.\end{cases} \tag{52}$$

One needs to be careful because the gradients of the steady-state concentration field diverge at the trijunction points. Details can be found in DL's article. Finally, the result is inserted in Eqs. (37). There are two types of contributions to linear order in ξ_j^s and y_j^s: the steady-state diffusion field is evaluated at the position of the perturbed interface, and the perturbed diffusion field is taken at the location of the steady-state interface. These different terms, containing sums over the steady-state interlamellar diffusion modes, lead to quite complicated expressions, summarized in Appendix A.

The calculation of $\tilde{\mathbf{U}}$ is somewhat easier because, with the assumption of equal solute partition coefficients, the steady-state impurity diffusion field is translationally invariant along x, and hence the horizontal displacements y_j^s drop out of the calculation. It would be possible to include the interlamellar impurity diffusion in the expression for $\tilde{\mathbf{U}}$ by following the lines of the DL calculation for $\mathbf{U}$. We expect, however, as argued in the preceding section, that this would only lead to minor corrections.

The perturbed impurity diffusion field is written as

$$\tilde{u}(x,z,t)=\tilde{u}_0(z)+\delta\tilde{u}(x,z,t) \tag{53}$$

and expanded in Fourier modes,

$$\delta\tilde{u}(x,z,t)=\sum_p \tilde{b}_p \exp[ipx-\tilde{q}_p(z-\overline{z})+\omega t]. \tag{54}$$

To calculate the constants $\tilde{q}_p$, we use the quasistationary approximation of the impurity diffusion equation. In terms of the dimensionless impurity field $\tilde{u}$, the continuity equation at the interface takes the form

$$-\tilde{D}\left.\frac{\partial\tilde{u}}{\partial z}\right|_{z=\zeta}=(v_p+\dot{\zeta})[(1-k_E)\tilde{u}+k_E]. \tag{55}$$

We want to keep only terms that are linear in the displacements ξ_j^s or their time derivatives. Such terms come from several sources: the time derivative of ζ, the corrections δu in the diffusion field and its gradient, and from evaluating the steady-state diffusion field at the new interface position $\zeta(x,t)$. The equation of order 1 in the displacements becomes

$$\begin{aligned}-\tilde{D}\left.\frac{\partial^2\tilde{u}_0}{\partial z^2}\right|_{z=\overline{z}}(\zeta-\overline{z})-\tilde{D}\left.\frac{\partial\delta\tilde{u}}{\partial z}\right|_{z=\overline{z}}&\\ =\dot{\zeta}[(1-k_E)\tilde{u}_0(x,\overline{z})+k_E]+v_p(1-k_E)\left.\frac{\partial\tilde{u}_0}{\partial z}\right|_{z=\overline{z}}&\\ \times(\zeta-\overline{z})+v_p(1-k_E)\,\delta\tilde{u}(x,\overline{z},t).&\end{aligned} \tag{56}$$

We now insert the Fourier expansion (54) in the above equation, multiply both sides by $\exp(-ip'x)/N\lambda$, and integrate over x from 0 to $N\lambda$. With $\tilde{u}_0(x,z)=\exp(-2(z-\overline{z})/\tilde{l})$, this leads to

$$\begin{aligned}\tilde{b}_p e^{\omega t}\left[\tilde{q}_p-\frac{2}{\tilde{l}}(1-k_E)\right]=\frac{4k_E}{\tilde{l}^2}\frac{1}{N\lambda}\int_0^{N\lambda}e^{-ipx}\zeta(x,t)dx&\\ +\frac{1}{\tilde{D}}\frac{1}{N\lambda}\int_0^{N\lambda}e^{-ipx}\dot{\zeta}(x,t)dx.&\end{aligned} \tag{57}$$

To perform the integrals over x, we use the piecewise constant expression, Eq. (52), for $\zeta(x,t)$. As $\zeta-\overline{z}$ is already of order ξ, we can neglect the y's in the integration boundaries. For ξ_j^s given by a Fourier mode of wave number k according to Eqs. (41), we obtain

$$\begin{aligned}\tilde{b}_p=\left[\tilde{q}_p-\frac{2}{\tilde{l}}(1-k_E)\right]^{-1}\left(\frac{4k_E}{\tilde{l}^2}+\frac{\omega}{\tilde{D}}\right)\frac{e^{-ip\eta\lambda/2}}{p\lambda}&\\ \times\left[\sin\frac{p\eta\lambda}{2}(\tilde{X}_p^\alpha+\tilde{X}_p^\beta)\right.&\\ \left.+\sin\frac{p(1-\eta)\lambda}{2}(e^{ip\lambda/2}\tilde{X}_p^\alpha+e^{-ip\lambda/2}\tilde{X}_p^\beta)\right],&\end{aligned} \tag{58}$$

where

$$\tilde{X}_p^s=\frac{1}{N}\sum_{j=0}^{N-1}e^{-ip\lambda j-\omega t}\xi_j^s=\sum_n \delta_{p,k+2\pi n/\lambda}X_k^s \quad (s=\alpha,\beta). \tag{59}$$

Note that, even if we start with a set of ξ's given by a single Fourier mode of wave number k, the use of the piecewise constant interface shape of Eq. (52) induces perturbations in the diffusion field at all wave numbers shifted with respect to k by a multiple of $2\pi/\lambda$. This effect is unavoidable if we want to replace the full free boundary problem by equations for a discrete set of variables.

The next step is the calculation of the average concentrations in front of each lamella:

$$\delta\langle\tilde{u}\rangle_j^\alpha(t)=\frac{1}{\eta\lambda}\int_{j\lambda}^{(j+\eta)\lambda}\left(\left.\frac{\partial\tilde{u}_0}{\partial z}\right|_{z=\overline{z}}\langle\xi\rangle_j^\alpha+\delta\tilde{u}(x,\overline{z},t)\right)dx \tag{60a}$$

$$\begin{aligned}\delta\langle\tilde{u}\rangle_j^\beta(t)=\frac{1}{(1-\eta)\lambda}&\\ \times\int_{(j+\eta)\lambda}^{(j+1)\lambda}\left(\left.\frac{\partial\tilde{u}_0}{\partial z}\right|_{z=\overline{z}}\langle\xi\rangle_j^\beta+\delta\tilde{u}(x,\overline{z},t)\right)dx.&\end{aligned} \tag{60b}$$

The first term inside each integral is due to the displacement of the interface in the steady-state diffusion field, and the second arises from the perturbed diffusion field evaluated at the steady-state interface position. The final result for the matrix $\tilde{\mathbf{U}}$ is

$$\tilde{\mathbf{U}}^{\alpha,\alpha}=-\frac{1}{\tilde{l}}+\frac{1}{\eta\tilde{l}}\left(\frac{2k_E\lambda}{\tilde{l}}+\frac{\omega\lambda\tilde{l}}{2\tilde{D}}\right)[\tilde{S}_1(\kappa,\eta)+\tilde{S}_2^*(\kappa,\eta)], \tag{61a}$$

$$\tilde{\mathbf{U}}^{\alpha,\beta}=\tilde{\mathbf{U}}^{\alpha,\alpha *}, \tag{61b}$$

$$\tilde{\mathbf{U}}^{\beta,\beta}=-\frac{1}{\tilde{l}}+\frac{1}{(1-\eta)\tilde{l}}\left(\frac{2k_E\lambda}{\tilde{l}}+\frac{\omega\lambda\tilde{l}}{2\tilde{D}}\right)[\tilde{S}_1(\kappa,1-\eta)+\tilde{S}_2^*(\kappa,1-\eta)], \tag{61c}$$

$$\tilde{\mathbf{U}}^{\beta,\alpha}=e^{ik\lambda}\tilde{\mathbf{U}}^{\beta,\beta *}, \tag{61d}$$

where $\tilde{\mathbf{U}}^{\alpha,\alpha *}$ denotes the expression obtained from $\tilde{\mathbf{U}}^{\alpha,\alpha}$ by complex conjugation of all quantities except for ω (for ω real, this is the usual complex conjugation), and we have defined

$$\kappa=k\lambda/2\pi, \tag{62}$$

$$r=l/\tilde{l}=D/\tilde{D}, \tag{63}$$

$$\tilde{\rho}_n(\kappa)=\sqrt{r^2\mathrm{Pe}^2+4\pi^2(n+\kappa)^2}-r\,\mathrm{Pe}+2rPek_E, \tag{64}$$

$$\tilde{S}_1(\kappa,\eta)=\sum_{n=-\infty}^{\infty}\frac{\sin^2[\pi\eta(n+\kappa)]}{\pi^2(n+\kappa)^2\tilde{\rho}_n(\kappa)}, \tag{65}$$

$$\tilde{S}_2(\kappa,\eta)=\sum_{n=-\infty}^{\infty}e^{-i\pi(n+\kappa)}\times\frac{\sin[\pi\eta(n+\kappa)]\sin[\pi(1-\eta)(n+\kappa)]}{\pi^2(n+\kappa)^2\tilde{\rho}_n(\kappa)}. \tag{66}$$

These notations have been chosen in analogy to some of DL's results (see Appendix A). The ratio r of the eutectic and impurity diffusion lengths is usually close to 1, and κ is the dimensionless wave number. For small Péclet numbers, and perturbation wavelengths much larger than the lamellar spacing ($\kappa\ll 1$), the sums $\tilde{S}_1$ and $\tilde{S}_2$ are dominated by the term with $n=0$. In this limit, we can neglect all the other terms in the sums, which corresponds to keeping only the Fourier coefficient $\tilde{b}_p$ with $p=k$, and hence to a single-mode approximation of the perturbed impurity diffusion field. When κ is larger, however, and in particular near the ''Brillouin zone'' boundary, $\kappa=0.5$, we have to consider the full sums. To obtain the stability spectra, we must now combine this result with DL's calculations for the other matrices and solve the characteristic equation for ω.

V. SYMMETRIC PHASE DIAGRAM AT EUTECTIC COMPOSITION

A. Stability spectrum

In general, the characteristic equation of the stability spectrum is a polynomial of degree four in ω with real coefficients. The solutions could be obtained algebraically, but this method leads to complicated expressions that are difficult to interpret. For this reason, we will restrict our attention in this section to the special case of an alloy of eutectic composition in a model system where the phase diagram is symmetrical about the eutectic composition. In this case, the characteristic equation can be factored into two quadratic equations, thus greatly simplifying the interpretation. As we shall see when we treat the general case in Sec. VI, all qualitative features of the instability are already contained in this special case.

There are general relations between the elements of the matrix $\mathbf{A}$, due to the existence of two planes of mirror symmetry in the steady state, one in the middle of each type of lamella (α or β). Hence we can change the sign of k and relabel the trijunction points without affecting the final result. This leads to the relations

$$\mathbf{A}^{\alpha,\beta}=\mathbf{A}^{\alpha,\alpha *}, \tag{67a}$$

$$\mathbf{A}^{\beta,\alpha}=e^{ik\lambda}\mathbf{A}^{\beta,\beta *}. \tag{67b}$$

Here, an asterisk again denotes complex conjugation of all quantities except ω. If we consider a model eutectic with a completely symmetric phase diagram, i.e., $m_\alpha=m_\beta=m$, $\tilde{m}_\alpha=\tilde{m}_\beta=\tilde{m}$, $\Gamma_\alpha=\Gamma_\beta=\Gamma$, $\theta_\alpha=\theta_\beta=\theta$, and $u_\beta=-u_\alpha=1/2$, at its eutectic composition, $\eta=1/2$, we have in addition $\mathbf{A}^{\alpha,\alpha}=\mathbf{A}^{\beta,\beta}$. The solvability condition, $\det\mathbf{A}=0$, can then be factored into two equations,

$$\mathrm{Re}(e^{-ik\lambda/4}\mathbf{A}^{\alpha,\alpha})=0 \quad \text{and} \quad \mathrm{Im}(e^{-ik\lambda/4}\mathbf{A}^{\alpha,\alpha})=0, \tag{68}$$

both of them quadratic in ω.

To proceed, we will rewrite the equations in a dimensionless form. For the sake of subsequent generalization, we will give expressions for the parameters that are valid for any phase diagram. We define

$$M=\frac{m_\alpha m_\beta}{(m_\alpha+m_\beta)/2}, \tag{69}$$

$$\Omega=\omega\lambda/v_p, \tag{70}$$

$$g=\frac{Gl}{M\Delta c}=\frac{2DG}{v_pM\Delta c}, \tag{71}$$

$$w=\frac{\tilde{m}\Delta\tilde{c}}{M\Delta c}, \tag{72}$$

$$\Lambda = \lambda/\lambda_{\min}. \tag{73}$$

Here, M is a mean liquidus slope (for the symmetric phase diagram, $M=m$); $1/\mathrm{Re}\,\Omega$ is the distance along the z direction that the interface needs to travel (in units of lamellar spacing) for the amplitude of the perturbation to grow by a factor of e; and $2\pi/\mathrm{Im}\,\Omega$ is the length traveled by the interface during one oscillation cycle. The parameter w is the ratio of the two freezing ranges and is proportional to the impurity concentration since $\Delta\tilde{c}=(1/k_E-1)\tilde{c}_\infty$.

It may be useful to comment on typical experimental values of the dimensionless parameters. The best studied system in this context is the organic eutectic CBr_4-C_2Cl_6 used originally by Hunt and Jackson [4]. This system contains naturally residual gas that acts as an impurity, leading to colony formation. For this system, Akamatsu and Faivre [34] have estimated w to be of order 0.1, with a distribution coefficient $k_E \approx 0.02$. The Péclet number Pe is typically between 0.01 and 0.1 in the low-velocity regime used to investigate colony formation.

After multiplication by $l\Omega/(M\Delta c)$, the first of Eqs. (68) becomes, expressed in the above dimensionless quantities (see Appendix A for more details),

$$\begin{aligned} 0 = {} & \Omega\frac{g}{2}\cos\frac{\pi\kappa}{2} + \frac{2P(\eta)}{\eta\Lambda^2}\sin(\pi\kappa/2)\sin(\pi\kappa)(\Omega\cot\theta - 2/\eta) \\ & + \Omega^2\,\mathrm{Re}[e^{-i\pi\kappa/2}U_1^\alpha(\kappa,\eta)] + \Omega\,\mathrm{Re}[e^{-i\pi\kappa/2}U_2^\alpha(\kappa,\eta)] \\ & + 2\sin(\pi\kappa)\mathrm{Re}[ie^{i\pi\kappa/2}U_3(\kappa,\eta)] - wr\Omega\cos\frac{\pi\kappa}{2} \\ & + \frac{wr\Omega}{\eta}(2k_E r\,\mathrm{Pe}+\Omega)\left(\tilde{S}_1(\kappa,\eta)\cos\frac{\pi\kappa}{2}\right. \\ & \left. + \mathrm{Re}[e^{-i\pi\kappa/2}\tilde{S}_2^\star(\kappa,\eta)]\right), \end{aligned} \tag{74}$$

where we have chosen to display η, for clarity, although the factorization is only possible for $\eta=1/2$. The first term of Eq. (74) arises from the matrix $\mathbf{G}$; the factor $\cos(\pi\kappa/2)$ is simply due to the averaging over the two trijunction points limiting a lamella. The matrix $\mathbf{K}$ contributes the next two terms, proportional to Λ^{-2}. The first, containing Ω, describes the change of curvature due to the bending of the interface over a large scale, and is therefore equivalent to the capillary term in the dilute binary alloy problem. The second gives the change in average curvature upon variation of the local lamellar spacing. All terms containing the functions $U_n^\alpha(\eta,\kappa)$, defined in Appendix A, are due to the eutectic diffusion field. Finally, the terms proportional to w arise from the matrix $\tilde{\mathbf{U}}$.

Equation (74) is exact and can be solved numerically. But it is also useful to simplify this equation in order to render the physical interpretation of the instability more transparent. To this end, let us group the terms with equal powers of Ω and rewrite Eq. (74) as

$$a(\kappa)\Omega^2 - b(\kappa)\Omega + c(\kappa) = 0. \tag{75}$$

To obtain a simplified expression, we expand the coefficients $a(\kappa)$, $b(\kappa)$, and $c(\kappa)$ in powers of κ. Details on this procedure can be found in Appendix B. It turns out that an expansion up to order κ^2 is sufficient to obtain a satisfying agreement with the direct numerical solution of Eq. (74). We obtain

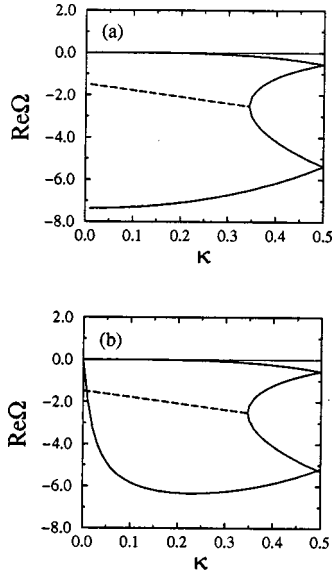

FIG. 5. Stability spectra of the symmetric eutectic at $\Lambda=1$, Pe $=0.01$, $g=1$, $r=1$, $k_E=0.05$, and $\theta=45°$ (a) without impurity ($w=0$) and (b) with a small amount of ternary impurity ($w=0.01$). Full lines, real modes; dashed lines, complex modes.

$$a(\kappa) = 2P(1/2) + \frac{wr}{\tilde{\rho}_0(\kappa)}, \tag{76a}$$

$$b(\kappa) = wr - g/2 - \left(\frac{2\pi^2 P(1/2)\cot\theta}{\Lambda^2} + \frac{R_0}{2}\right)\kappa^2 - \frac{2w\,\mathrm{Pe}\,r^2 k_E}{\tilde{\rho}_0(\kappa)}, \tag{76b}$$

$$c(\kappa) = 8\pi^2 P(1/2)\left(1 - \frac{1}{\Lambda^2}\right)\kappa^2, \tag{76c}$$

where $\tilde{\rho}_0(\kappa)$ is defined by Eq. (64), and R_0 is a constant given by Eq. (B11). We note that, to obtain these expressions, we have only kept the leading order terms of each of the contributions in Eq. (74) and dropped several terms of order $|\kappa|$ and κ^2 that turn out to give negligible contributions at the onset of instability for the reasons detailed in Appendix B. The simplified stability spectrum defined by the equations above will be used below to derive simple analytical expressions for the onset velocity and wavelength. Moreover, it will allow us to identify the terms that contribute to the effective surface tension in the long-wavelength free boundary formulation presented in Sec. VI. In the rest of this paper, the results based on this simplified spectrum will be systematically checked against the direct numerical solution of Eq. (74).

B. Binary versus ternary eutectic: The limit $\kappa \to 0$

Let us first examine the limit $\kappa \to 0$ of the stability spectrum, which governs the relaxation to steady-state growth after an infinitesimal translation of the solidification front along the z axis. Although this is not the limit of interest for morphological instability, it is worth a brief discussion to understand more fully the subtle effects of the ternary impurity on the complete stability spectrum.

Since, as mentioned above, the complete eigenvalue equation is of degree four in Ω with real coefficients, there are four branches of the dispersion relation, and modes can be real or occur in complex conjugate pairs. In the completely symmetric case, each of the two equations (68) gives a pair of branches. To calculate the stability spectra, we must first evaluate numerically the sums occurring in the functions $U_n(\kappa,\eta)$ to obtain the coefficients of the polynomial in Ω, which can then be solved for each κ. Figure 5 shows a comparison between the stability spectrum of a binary eutectic ($w=0$) and a eutectic with a small amount of impurities, ''small'' meaning that we stay far below the threshold of instability. We have chosen the parameters g and Λ in order to reproduce, for the binary eutectic, Fig. 4(b) of DL's article. Without impurities, we can distinguish two types of branches. There is always a characteristic diffusive branch, which is real and satisfies $\Omega \propto \mathcal{D}(\Lambda)\kappa^2$ for $\kappa \to 0$: the spacing can be locally adjusted by ''diffusion'' in λ space [23]. This branch is related to the long-wavelength lamella elimination instability for $\lambda < \lambda_{\min}$: the effective diffusion coefficient $\mathcal{D}(\Lambda)$ is negative for $\Lambda < 1$. The companion of this branch is also real, with strongly negative growth rates. The second pair of branches is complex for small κ. This mode gives rise to the 2λ-O instability for sufficiently off-eutectic compositions: it becomes complex up to the ''Brillouin zone'' boundary $\kappa = 0.5$ and its real part becomes positive.

When we add a small amount of impurities ($w=0.01$), we find that the diffusive and oscillatory branches are nearly unaffected; however, the companion of the diffusive branch undergoes a drastic change. Physically speaking, this strong reaction to a seemingly small perturbation is due to the introduction of a new conservation law. In the binary eutectic, this mode describes the relaxation of an interface by the motion of the trijunction points with respect to the temperature gradient (in the z direction). At the eutectic composition, this relaxation involves only short range interlamellar diffusion and is therefore fast. On the other hand, for a flat interface, the impurities must diffuse over a length scale of the order of the diffusion length to achieve relaxation. This leads to much slower decay rates for small wave numbers.

To see more formally how this change arises, let us consider Eqs. (76) in the limit $\kappa \to 0$. Without the impurity terms ($w=0$), $a(\kappa)$ and $b(\kappa)$ stay finite in the limit $\kappa \to 0$, whereas $c(\kappa) \propto \kappa^2$. Hence $\Omega \propto \kappa^2$ leads to a balance between the last two terms of Eq. (75). In the impurity terms, we have $\tilde{\rho}_0(\kappa) \to 2k_E r\,\mathrm{Pe}$ for $\kappa \to 0$, and for $\kappa = 0$ we obtain

$$\left(2P(1/2) + \frac{w}{2k_E\,\mathrm{Pe}}\right)\Omega^2 - \frac{g}{2}\Omega = 0, \tag{77}$$

yielding the solutions, $\Omega = 0$, for the diffusive branch and, $\Omega = -g/[4P(1/2) + w/(k_E\,\mathrm{Pe})]$, for its companion. In the latter expression, the impurity contribution is dominant for small Péclet number and small impurity partition coefficient, and hence this branch is strongly influenced by the addition of impurities. As the terms proportional to $\tilde{\rho}_0(\kappa)^{-1}$ also appear in the classical Mullins-Sekerka analysis of a monophase solidification front, we will hereafter refer to this branch as the MS branch.

The oscillatory branch is little affected by the addition of impurities. The reason is that the second of Eqs. (68) does not contain the MS terms at $\kappa = 0$. We will discuss the relation between long- and short-wavelength instabilities in more detail in Sec. VII.

The derivation of Eqs. (74) and (76) is based on the quasistationary approximation of the two diffusion equations. This approximation relies on the assumption that the wavelength of the perturbation is smaller than the diffusion length, and hence breaks down for $\kappa \ll \mathrm{Pe}$. In the framework of the DL formalism, however, the calculation becomes extremely tedious if this assumption is relaxed, and the results of this calculation will not be displayed here. The effective interface formulation to be presented in Sec. VI, however, easily allows us to relax this assumption and to include the dynamics of the diffusive boundary layer. As a result, the MS branch of the spectrum becomes complex for $\kappa \ll \mathrm{Pe}$, corresponding to an oscillatory relaxation of the interface to steady-state growth driven by oscillations of the impurity boundary layer that is already well-known for a monophase front. As we shall see below, the morphological instability leading to colony formation involves only modes with $\kappa \gg \mathrm{Pe}$ for which the quasistationary approximation is valid.

C. Onset of instability

Let us now examine the onset of instability and compare our findings to the well-known results for dilute binary alloys. For the one-sided model, the constitutional supercooling (CS) criterion is fairly accurate. This criterion states that a monophase solidification front is unstable if the diffusion length is less than twice the thermal length $l_T = \tilde{m}\Delta\tilde{c}/G$. In our dimensionless variables, this is equivalent to $g < 2wr$. The Mullins-Sekerka analysis shows [10] that the actual critical velocity differs from CS by corrective factors that are usually small. The critical wavelength λ_c at the onset of instability scales as $\lambda_c \sim (d_0 l_T \tilde{l})^{1/3}$, where d_0 is the capillary length.

Let us briefly comment on some consequences of this scaling. From Eq. (28) we can deduce that the eutectic spacing $\lambda_{\min}$ scales as $\lambda_{\min} \sim (d_0 l)^{1/2}$. Therefore, for low Péclet numbers we always expect $\lambda_{\min} \ll \lambda_c$, and hence we can consider the limit of small κ for the determination of the onset of instability. On the other hand, λ_c will always be smaller than the diffusion length, and we have $k\tilde{l}/2\pi \gg 1$, or equivalently $\kappa \gg \mathrm{Pe}$. Therefore, we may use the simplification $\tilde{\rho}_0(\kappa) \approx 2\pi|\kappa|$ in Eqs. (76).

The occurrence of unstable modes is determined by the behavior of $b(\kappa)$: if $wr - g/2$ is positive and large enough, $b(\kappa)$ becomes positive for a certain range in κ. We want to determine the critical value g_c of the parameter g where the first unstable mode occurs, and the wave number κ_c of this mode. The two solutions of the quadratic equation (75) are

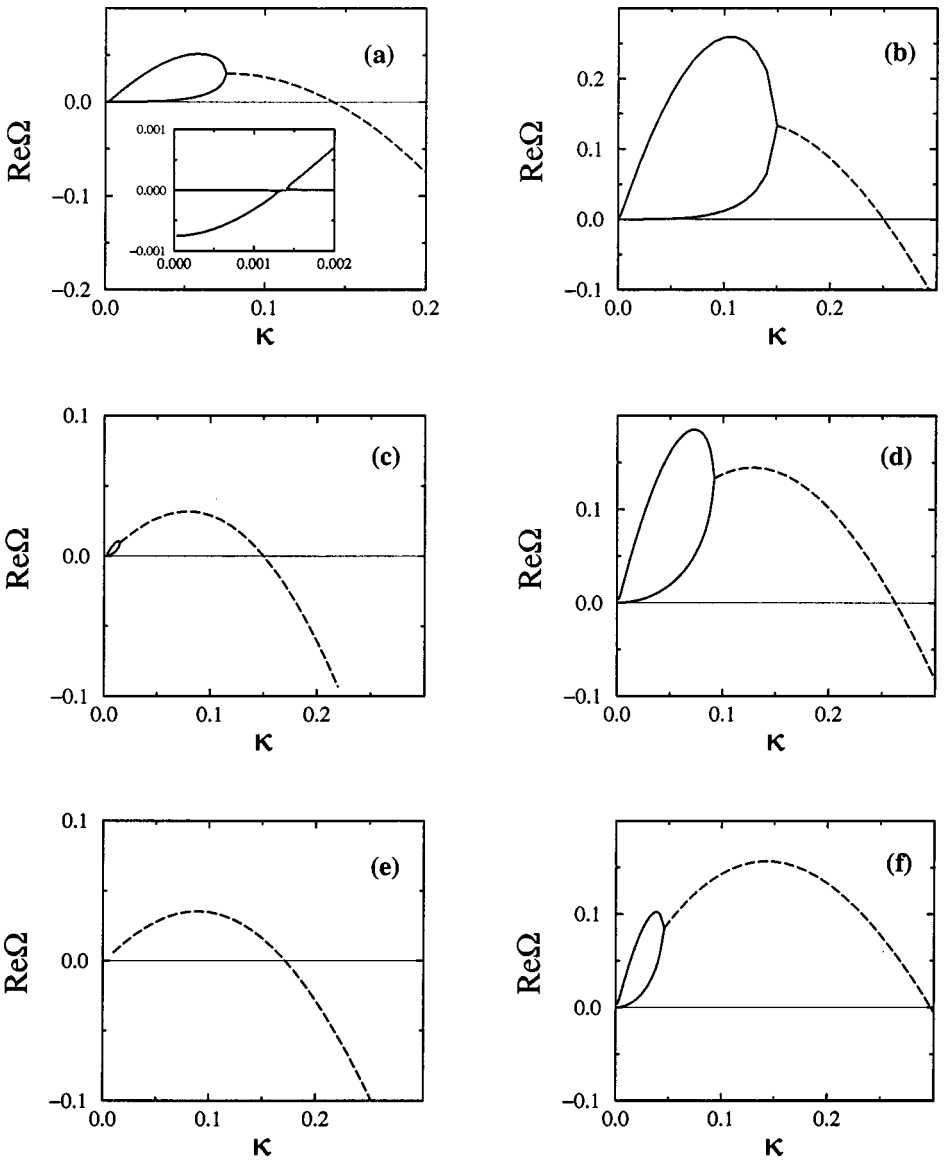

FIG. 6. Stability spectra for varying g and Λ and $w=0.1$, Pe $=0.01$, $r=1$, $k_E=0.05$, and $\theta=45°$. (a) $g=0.15$, $\Lambda=1$; (b) $g=0.05$, $\Lambda=1$; (c) $g=0.15$, $\Lambda=1.1$; (d) $g=0.05$, $\Lambda=1.1$; (e) $g=0.15$, $\Lambda=1.5$; (f) $g=0.05$, $\Lambda=1.5$. Solid lines, real modes; dashed lines, complex modes. Note that we show only the diffusive and MS branches in the region of small κ where they are unstable. The inset in (a) shows in more detail the part of the spectrum at small κ.

$$\Omega_{\pm}=\frac{b(\kappa)\pm\sqrt{b^2(\kappa)-4a(\kappa)c(\kappa)}}{2a(\kappa)}. \tag{78}$$

As the product $a(\kappa)c(\kappa)$ is always positive and finite, the solutions become complex when $b(\kappa)$ tends to 0, and we have $\mathrm{Re}\,\Omega=b(\kappa)/2a(\kappa)$. Hence the two conditions to obtain g_c and κ_c are simply $b(\kappa)=0$ and $db(\kappa)/d\kappa=0$. Let us rewrite the first of these conditions in the dimensional quantities and divide through by wr. The result is

$$1-\frac{G\tilde{D}}{\tilde{m}\Delta\tilde{c}v_p}-\frac{\Gamma\tilde{l}\cos\theta}{\tilde{m}\Delta\tilde{c}}\frac{k^2}{2}-\frac{R_0\lambda^2}{4\pi^2 wr}\frac{k^2}{2}-\frac{2k_E}{k\tilde{l}}=0. \tag{79}$$

There are two terms proportional to k^2. The first is the surface tension term, which stabilizes the interface. It is analogous to the surface tension term in the monophase MS spectrum, except that it is multiplied by a geometrical factor $\cos\theta$. This factor is present because the eutectic interface is made of an array of arcs, each one linking two trijunctions, which renders the front less stiff than a flat monophase interface. The second term arises from the eutectic diffusion field. It can be directly interpreted by noting that the above equation becomes identical to the result for a monophase planar interface if we define the effective capillary length

$$\bar{d}_0=\frac{\Gamma\cos\theta}{\tilde{m}\Delta\tilde{c}}+\frac{R_0\,\mathrm{Pe}\,\lambda}{4\pi^2 w}. \tag{80}$$

The above expression implies that the interlamellar eutectic diffusion field has a stabilizing effect. This is rather remarkable since it implies that the two diffusion fields (associated with the eutectic components and the ternary impurities, respectively) play antagonistic roles in the instability.

From the condition $db(\kappa)/d\kappa=0$ we obtain the expression

$$k_c^3=\frac{2k_E}{\bar{d}_0\tilde{l}^2} \tag{81}$$

for the critical wave number. Furthermore, substituting this expression in Eq. (79), we find

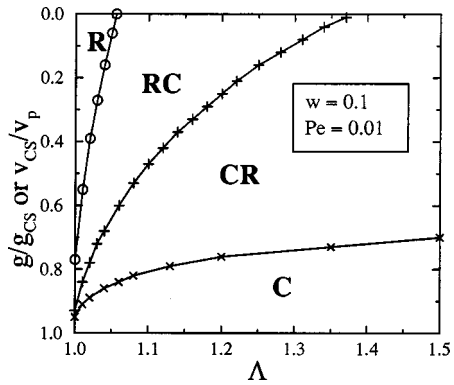

FIG. 7. Structure of the dispersion relation as function of the parameters $\Lambda=\lambda/\lambda_{\min}$ and $g/g_{\mathrm{CS}}=v_{\mathrm{CS}}/v_p$. The onset of instability (constitutional supercooling) is at the bottom of the diagram. The meanings of R, RC, CR, and C are defined in the text.

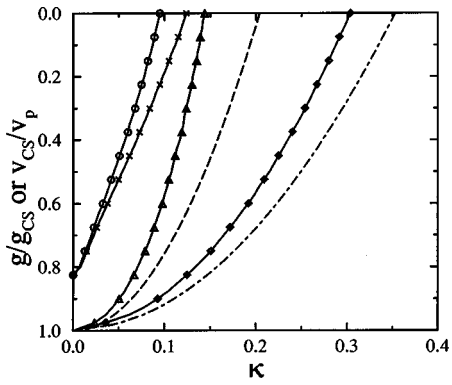

FIG. 8. Wave numbers of some characteristic points in the stability spectrum as a function of g/g_{CS} for $w=0.1$, Pe$=0.01$, $k_E=0.05$, and $\Lambda=1.1$. Solid lines with circles, real maximum; with crosses, limit between real and complex modes; with triangles, complex maximum; and with diamonds, marginally stable mode. The dashed and dash-dotted lines are the approximations for the complex maximum and the marginal mode given by Eqs. (83) and (85), respectively.

$$v_c=\frac{G\tilde{D}}{\tilde{m}\Delta\tilde{c}}\,\frac{1}{1-3(\bar{d}_0k_E^2/2\tilde{l})^{1/3}} \tag{82}$$

for the critical pulling speed. This expression is equivalent to the constitutional supercooling criterion ($v_{CS}=G\tilde{D}/\tilde{m}\Delta\tilde{c}$) up to the capillary correction in the denominator of the second term on the RHS of Eq. (82). This correction is typically negligibly small, except for very low impurity concentrations where the effective capillary length becomes large. Consequently, as for a monophase front, there is a critical impurity concentration below which the eutectic front is completely stable.

The above results show that the instability of the eutectic interface is qualitatively similar to the standard MS instability of a monophase front, as far as the expressions for k_c and v_c are concerned, up to a renormalization of the surface tension as described by Eq. (80). One main difference, however, is that the branch of the spectrum that becomes unstable is complex, which suggests the existence of oscillatory patterns with a wavelength much larger than the lamellar spacing. To decide whether such patterns are observable experimentally, we need to examine next how this complex branch evolves above the onset of instability.

D. Above onset

For $v>v_c$, the solutions for Ω still satisfy the quadratic equation (75). The nature of the mode, whether complex or real, is determined by the sign of the discriminant, $b^2(\kappa)-4a(\kappa)c(\kappa)$. The most important parameter, besides g, that controls the discriminant is Λ, because $c(\kappa)$ strongly depends on Λ near $\Lambda=1$. We are interested only in the case $\Lambda>1$, since spacings below $\lambda_{\min}$ are intrinsically unstable. For Λ near 1, $c(\kappa)$ is small, and real modes should appear. In contrast, for larger Λ, complex modes should be favored.

To check this prediction, we plot in Fig. 6 a series of stability spectra, calculated using Eq. (74), for varying g and Λ. We chose $w=0.1$, which, using the constitutional supercooling criterion, gives a critical temperature gradient of $g_{CS}=0.2$. We display spectra for two values of g, one close to onset ($g=0.15$), and one far above the onset ($g=0.05$).

Let us first comment on the structure of the spectrum at small values of κ. The inset of Fig. 6(a) shows that the growth rate still satisfies Eq. (77) for $\kappa=0$, but now as κ grows the MS branch and the diffusive branch meet to form a complex conjugate pair, because $b(\kappa)$ approaches zero and the discriminant becomes negative. When κ grows further, the real part of Ω becomes positive, and the branch may stay complex or split again in two real branches, both with positive growth rates. For $\Lambda=1$ [Figs. 6(a) and 6(b)], the spectra always exhibit real modes above the onset, and the mode with the maximum growth rate is real for both values of g. For $\Lambda=1.1$ [Figs. 6(c) and 6(d)], near the onset only a narrow band of real modes is present, and the fastest growing mode is complex. This changes at lower g: the κ range of real modes has increased, and the fastest growing mode is real. Note that in both spectra there are two maxima of the growth rate, one real and the other complex. At a certain value of g, the two maxima are of equal height; at this point, we have a finite jump in the wave number of the fastest growing mode when g is varied, and two perturbations of different wave numbers grow with the same rate. Finally, for $\Lambda=1.5$ [Figs. 6(e) and 6(f)], there is a range of g where the spectrum is entirely complex, and only far above the onset do real modes appear. The fastest growing mode is always complex.

We can summarize these results in a diagram that shows the nature of the spectrum in the plane (Λ,g) (Fig. 7). For this diagram, we normalize the temperature gradient by its critical value according to the constitutional supercooling criterion, $g_{\mathrm{CS}}=2rw$. Note that we have $g/g_{\mathrm{CS}}=v_{\mathrm{CS}}/v_p$, where $v_{CS}=G\tilde{D}/\tilde{m}\Delta\tilde{c}$ is the critical velocity. We classify the spectra into four categories, according to the occurrence of maxima. We denote by R spectra with only a real maximum [Fig. 6(a)]; spectra with a real and a complex maximum are denoted by RC when the fastest growing mode is real [Fig. 6(d)], and by CR when it is complex [Fig. 6(c)]. Finally, the entirely complex spectra are denoted by C. Figure 7 shows for which parameters we can expect predominantly real or complex modes; around the line between RC and CR, we can have the competition of two different modes. This diagram was determined using Eq. (74) with the

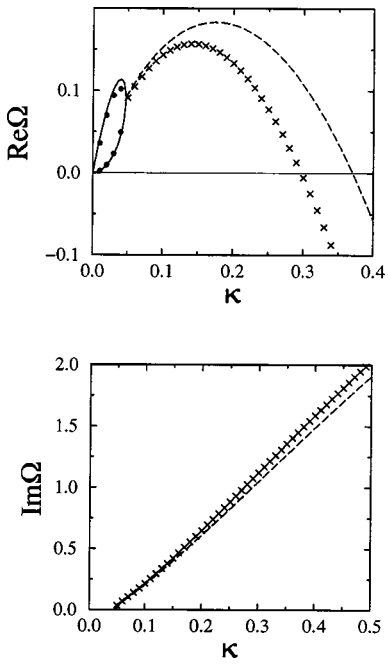

FIG. 9. Comparison of stability spectra obtained by the full calculation, Eq. (74), and by Eq. (75) using Eqs. (76) for the coefficients a, b, and c. Symbols, full calculation (circles, real modes; crosses, complex modes). Lines, approximation (solid lines, real modes; dashed lines, complex modes). The parameters are the same as for Fig. 6(f).

parameters $w=0.1$, Pe$=0.01$, and $k_E=0.05$. Increasing the concentration of impurities (increasing w) favors real modes: all curves are shifted to the right and to the bottom in the diagram. The Péclet number and the partition coefficient influence the diagram only in the part near the onset of instability.

To describe a spectrum in more detail, we may use several characteristic wave numbers: the wave numbers of the fastest growing modes, the limit between real and complex modes, and the wave number of the marginally stable mode κ_m. Figure 8 shows these quantities as a function of g for $\Lambda=1.1$. As can be seen from Figs. 6(c) and 6(d), for this value of Λ real modes become dominant only well beyond the CS threshold.

To investigate systematically these quantities as functions of the control parameters, it is cumbersome to use Eq. (74) because of the sums involved in the functions U_n. Therefore, it is convenient to obtain approximate expressions for the wave numbers of the marginal mode and the complex maximum using the approximate spectrum defined by Eq. (75) and Eqs. (76). We will show in Sec. VI that this simplified spectrum can be recovered from an effective interface approach, which applies to an arbitrary phase diagram and composition. It is therefore worthwhile to investigate the quality of this approximation in the present symmetric case by quantitative comparison with the exact spectrum of Eq. (74). Figure 9 shows that, for the example of the last spectrum in Fig. 6, the qualitative aspect of the spectrum is well reproduced. We checked several cases and always found that the approximation shifts the marginally stable mode and the maxima to larger κ. The error, however, never exceeded about 30%. The imaginary part of Ω is very well approximated over the whole range of κ. We also recalculated the diagrams of Figs. 7 and 8, and found that the lines are slightly shifted, but the qualitative structure of the diagrams stays the same. It seems therefore valid to use Eqs. (76) for a general analysis.

The marginally stable mode is always complex, and κ_m can be determined by the condition $b(\kappa_m)=0$. In addition, far enough above the onset the term in $1/\kappa$ in Eq. (76b) can be neglected. We find

$$\kappa_m^2=\frac{1}{\alpha}\left(wr-\frac{g}{2}\right) \tag{83}$$

with

$$\alpha=\frac{2\pi^2 P(1/2)\cot\theta}{\Lambda^2}+R_0=\frac{4\pi^2 wl}{\lambda^2}\bar{d}_0, \tag{84}$$

where R_0, as before, is given by Eq. (B11). We can also give an approximate expression for the wave number of the complex maximum. For complex modes, $\mathrm{Re}\,\Omega=b(\kappa)/2a(\kappa)$. If we neglect the first term in Eq (76a) for $a(\kappa)$, we obtain

$$\kappa_{\max}\approx\kappa_m/\sqrt{3}=\sqrt{\frac{1}{3\alpha}\left(wr-\frac{g}{2}\right)}. \tag{85}$$

The resulting curves for κ_m and $\kappa_{\max}$ are shown in Fig. 8. For the real maximum, all terms in the quadratic equation for Ω have to be retained, and no simple expression for the wave number of the maximum can be obtained.

Some remarks seem to be in order here to clarify the meaning of Eq. (83) in the dimensional variables. Since $g/g_{CS}=v_{CS}/v_p$, the limit of high pulling speeds corresponds to $g\to 0$. In this limit, the structure of the spectrum varies very little with the pulling speed, because both the characteristic length of the MS problem, $\sqrt{d_0\tilde{l}}$ and the spacing $\lambda_{\min}$ vary as $1/\sqrt{v_p}$ far above the onset. Hence, if we increase the pulling speed and *at the same time* change the lamellar spacing such that Λ stays constant, the only parameter that changes (except g) is the Péclet number. But Pe appears in the problem only in the last term of Eq. (76b), which we have neglected in order to obtain Eq. (83). This term becomes important only at very high pulling speeds and leads to the absolute stability of the interface, as in the case of a dilute binary alloy. Substituting $\kappa=k\lambda/2\pi$ in Eq. (84) shows that, for constant Λ, far above the CS threshold the wavelength of the fastest growing complex mode scales as $\sqrt{\bar{d}_0 l}$, as for monophase solidification. On the other hand, in experiments on eutectics unstable states are usually reached from stable states by a sudden increase of the pulling velocity [27,28]. The lamellar spacing immediately after the jump is the same as before, but $\lambda_{\min}$ and consequently Λ have changed. Hence, starting from the same initial state and varying the final pulling speed corresponds to a variation of both g and Λ. Eq. (83) still applies, but in view of Eq. (84) no simple scaling with v_p is expected. A last remark concerns the dependence of κ_m on the impurity content. Taking the limit $g\to 0$ in Eq. (83) shows that $\kappa_m\sim\sqrt{w}\sim\sqrt{\tilde{c}_\infty}$. The reason for this behavior is that the effective capillary length, Eq. (80), scales as $\bar{d}_0\sim w^{-1}$, whereas $\lambda_{\min}$ is independent of w.

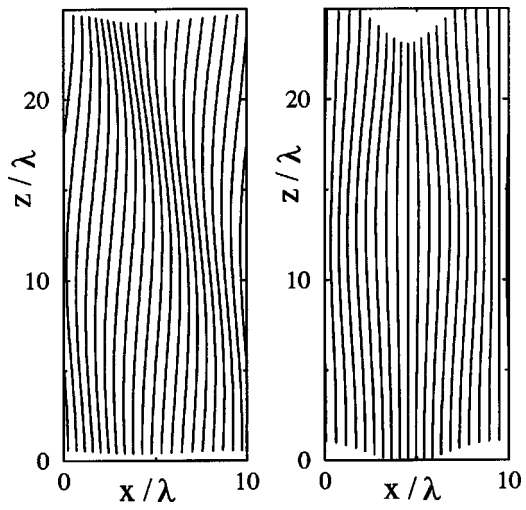

FIG. 10. Microstructures created by complex linear growth modes. Left, a single mode traveling to the left; right, a standing wave mode obtained by the superposition of two complex conjugate modes. Growth direction from bottom to top.

This means that the MS instability length increases with decreasing w, whereas the lamellar spacing stays constant, and hence we expect the wavelength of the primary instability of a eutectic front to decrease with increasing impurity content.

Finally, let us verify that the quasistationary approximation we have used to obtain the above results is justified. To this end, we estimate the order of magnitude of the three terms in the diffusion equation, Eq. (7a). For a perturbation δu of wave number $k>1/\tilde{l}$ ($\kappa>$Pe) growing at rate ω, we have $\partial_t \delta u \sim \omega \delta u$, $\partial_z \delta u \sim k \delta u$, and $\vec{\nabla}^2 \delta u \sim k^2 \delta u$. In terms of the dimensionless variables, the magnitude of these terms is $|\Omega|$Pe, κPe, and κ^2. From Fig. 9 we see that, for $\kappa>$Pe, $|\Omega|<B\kappa$ with some number B of order unity, and hence the omission of the time derivative from the diffusion equation is well justified for the range $\kappa>$Pe of interest here. It is also possible to relax the quasistationary approximation. Then, the growth rate ω appears in the denominators of all the sums $S_n(\kappa)$ and $\tilde{S}_n(\kappa)$. An analytic treatment becomes impossible, but the equation for Ω can be iterated numerically. We have checked that for the present range of parameters, the use of this complete calculation leads only to insignificant changes in the spectra. Note, however, that for higher Péclet numbers it may be necessary to include this effect.

E. Oscillatory modes

The most interesting result of this analysis is evidently the existence of complex modes. To illustrate the type of microstructures these modes would generate, we have calculated the trajectories of the trijunction points for a particular example, using the definitions, Eqs. (41), and the complex amplitudes X_k^s and Y_k^s obtained from the eigenvalue equation. For the symmetric alloy at the eutectic composition, the symmetry between the α and β phases gives immediately $X_k^\beta = \exp(ik\lambda/2) X_k^\alpha$. The amplitude and phase of X_k^α may be chosen arbitrarily, as this amounts to fixing the origins of the space and time axes. The Y_k^s were then calculated using the growth constraints Eqs. (40).

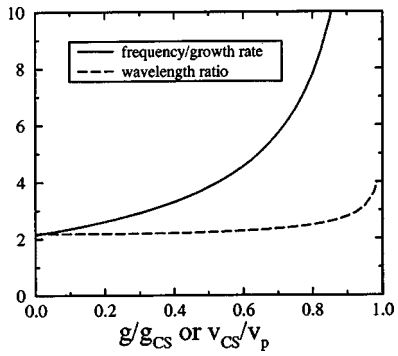

FIG. 11. Ratio of oscillation frequency to amplification rate, $\mathrm{Im}\,\Omega/\mathrm{Re}\,\Omega$, and ratio of the wavelengths in the z and x direction, $2\pi\kappa/\mathrm{Im}\,\Omega$, for the oscillatory modes with maximum growth rates as a function of g/g_{CS}. Other parameters are $\Lambda=1.5$, $w=0.1$, Pe $=0.01$, $k_E=0.05$.

We chose the complex modes with a maximum growth rate of Fig. 6(e) ($w=0.1$, $\Lambda=1.5$, $g=0.15$). As for every point in the complex part of the spectrum, there are two ''degenerate'' modes with complex conjugate growth rates. The modes of our example have a wavelength of 10λ ($\kappa=0.1$) and growth rates $\Omega=0.0347\pm0.257i$. One of these two modes is depicted in the left part of Fig. 10. We see that it has a ''traveling wave'' structure. The wavelength in the z direction, expressed in lamellar spacings, is $2\pi/\mathrm{Im}\,\Omega$, and the propagation velocity is $v/v_p=\mathrm{Im}\,\Omega/2\pi\kappa$. There are two complex conjugate modes: one propagates to the left, and the other to the right. As their growth rates are equal, we can create any superposition of the two, in particular a ''standing wave'' shown in the right part of Fig. 10.

The reason for the existence of these oscillatory modes is the interplay between the destabilizing impurity diffusion field and the dynamical response of the internal lamellar structure. A protrusion of the interface rejects impurities more efficiently than a flat interface, and hence grows faster. But as the curvature of the front increases, the trajectories of the trijunctions are more and more curved, and the local spacing increases. This leads to a decreased efficiency of the interlamellar eutectic diffusion and, hence, the interface slows down. As a result, the protrusion grows back. The lamellar spacing, however, still increases due to the geometric constraints, and the process overshoots, leading to a concave deformation of the front. This gives a geometric interpretation of the difference between traveling and standing waves: for the traveling wave, the lamellar spacings to the right and to the left of the protrusion are different, providing a driving force for the propagation of the perturbation. For the standing wave, the interface shape and the spacing are ''in phase,'' and the perturbation oscillates without propagation. Hence, the resulting microstructure depends on the initial relation between interface shape and lamellar spacing. This implies that in an experiment, where the initial perturbations of interface position and lamellar spacing have no reason to be in a particular phase relation, one should observe all possible superpositions.

There are two characteristic quantities (besides the wave number) related to an oscillatory mode: its propagation velocity, or equivalently the ratio of the wavelengths in the z and x directions, $2\pi\kappa/\mathrm{Im}\,\Omega$, and the ratio of its frequency

and its amplification time, $\mathrm{Im}\,\Omega/\mathrm{Re}\,\Omega$, which determines how many oscillations should be observable before the amplification leads to lamella elimination. In Fig. 11 we show both quantities as a function of g for $\Lambda=1.5$, where complex modes always dominate. We used Eqs. (75) and (76), determined for each value of g the wave number of the fastest growing mode, and calculated $\mathrm{Re}\,\Omega$ and $\mathrm{Im}\,\Omega$ at this point. Approximate values could be obtained by using Eq. (85) to obtain $\kappa_{\max}$. Figure 11 shows that the ratio of frequency and amplification rate diverges when we approach the onset. This is to be expected, as the growth rate vanishes, whereas the imaginary part of Ω remains finite. With decreasing g, fewer and fewer oscillations are observable before lamella terminations occur. However, even at $g=0$, more than two oscillations are completed before the amplitude of the mode has grown by a factor e, which means that such modes should be transiently observable. The amplification ratio generally increases when w decreases or Λ increases. The ratio of the wavelengths is fairly constant and slightly increases when Λ decreases or w increases.

VI. EFFECTIVE INTERFACE APPROACH

The discrete analysis of Sec. IV can in principle be used to calculate the stability properties of a eutectic front for an arbitrary phase diagram and composition. As we have seen, however, the resulting eigenvalue equation is quite complicated. It is therefore advantageous to develop an alternate formulation of the stability problem by exploiting the fact that the instability wavelength is typically much larger than the lamellar spacing. The idea, therefore, is to consider the shape of the large-scale front instead of the actual lamellar interface, and to solve a modified free boundary problem for this ''effective interface,'' with boundary conditions that account for the effect of the underlying lamellar structure.

It is useful to present this approach in two steps. In a first step, we write down the free boundary problem for the effective interface in the absence of surface tension effects. This yields a rigorous long-wavelength limit where the expression for Ω agrees up to order κ^2 with the one obtained from taking the small κ limit of the full discrete spectrum. This expression also reduces, in the absence of a ternary impurity, to the one derived by Langer [23] for a binary eutectic, and contains the long-wavelength instability leading to lamella termination for $\Lambda<1$. In a second step, we introduce phenomenologically the effect of surface tension guided by the insights of Sec. V. In the following, we will allow the volume fraction η and the eutectic liquidus slopes m_α and m_β to be arbitrary, and we will only require for brevity of notation that $\tilde{m}_\alpha=\tilde{m}_\beta$. We will briefly comment on the general case, where $\tilde{m}_\alpha\neq\tilde{m}_\beta$, at the end of this section.

A. Long-wavelength limit

We start by defining the effective interface as the continuous curve $\xi(x,t)$ that interpolates between the displacements of the trijunction points ξ_j^α and ξ_j^β and a continuous field $y(x,t)$ for the displacements along the x direction. To obtain the free boundary problem that governs the large-scale motion of this interface, we start by writing the diffusion equation for the ternary impurity in the liquid phase and the associated mass conservation condition at the phase boundary, which yields the equations

$$\partial_t\tilde{c}=\tilde{D}\nabla^2\tilde{c}, \tag{86}$$

$$-\tilde{D}\partial_n\tilde{c}=(v_p+\dot{\xi})(1-k_E)\tilde{c}, \tag{87}$$

where k_E is given by Eq. (16), and we have used in Eq. (87) the expression for the normal interface velocity in the moving frame, $v_n=v_p+\dot{\xi}$, which is valid for small amplitude deformations of the interface. Next, we need a boundary condition for $\tilde{c}$ on this interface. For this purpose, we note that lamellae can be assumed to grow locally in steady state as long as the interface deformation is on a scale much larger than the lamellar spacing. Therefore, we can assume that for such deformations, $\tilde{c}$ obeys locally the Gibbs-Thomson condition

$$T=T_E-\tilde{m}\tilde{c}-\Delta T_{JH}(\lambda,v_n), \tag{88}$$

where the contribution of the eutectic structure to the interfacial undercooling is given by the Jackson-Hunt formula

$$\Delta T_{\mathrm{JH}}(\lambda,v_n)=\frac{1}{2}\Delta T_{\min}\left(\frac{\lambda}{\lambda_{\min}}+\frac{\lambda_{\min}}{\lambda}\right), \tag{89}$$

with $\Delta T_{\min}$ and $\lambda_{\min}$ given by Eqs. (27) and (28). Finally, to complete the problem, we need to relate the local lamellar spacing $\lambda(x,t)$ and the shape of the front $\xi(x,t)$. This is done, as in Ref. [23], by noting that the local lamellar spacing is given by

$$\lambda(x,t)\approx\lambda_0\left(1+\frac{\partial y}{\partial x}\right), \tag{90}$$

for $y\ll\lambda$ where λ_0 is the unperturbed spacing. The field y can then be eliminated by using the geometrical constraint that lamellae grow locally perpendicular to the solidification front, which, expressed in terms of the continuous fields, takes the form

$$\frac{\partial y(x,t)}{\partial t}=-v_p\frac{\partial\xi}{\partial x}. \tag{91}$$

Equations (86)–(91), together with the boundary condition $\tilde{c}=\tilde{c}_\infty$ far from the interface, define the free boundary problem for small amplitude and long-wavelength deformations of the effective interface.

The stability spectrum can now be obtained by carrying out a standard linear stability analysis of the above equations, which is analogous to the analysis for a monophase front with the added ingredient that the Gibbs-Thomson condition is coupled to a slow evolution equation for $\lambda(x,t)$ obtained by combining Eqs. (90) and (91).

We start the stability analysis by writing the perturbations ξ and y in terms of Fourier modes,

$$\xi(x,t)=\xi_k\exp(ikx+\omega t), \tag{92a}$$

$$y(x,t)=y_k\exp(ikx+\omega t). \tag{92b}$$

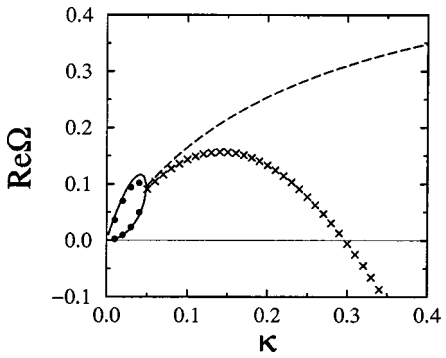

FIG. 12. Comparison between the full calculation and the long-wavelength limit, Eq. (97), for the stability spectrum. Symbols, full calculation, Eq. (74); circles, real modes; crosses, complex modes. Lines, long-wavelength limit, Eq. (97); solid lines, real modes; dashed lines, complex modes. The parameters are the same as for Figs. 6(f) and 9.

The impurity diffusion field is expanded in Fourier modes according to Eq. (54) and, carrying out the same steps as from Eqs. (54) to (58), allows us to determine the Fourier coefficients. As a result, Eq. (58) is replaced by

$$\tilde{b}_k=\left[\tilde{q}_k-\frac{2}{\tilde{l}}(1-k_E)\right]^{-1}\left(\frac{\omega}{\tilde{D}}+\frac{4k_E}{\tilde{l}^2}\right)\xi_k \tag{93}$$

with

$$\tilde{q}_k=\frac{1}{\tilde{l}}+\sqrt{\frac{1}{\tilde{l}^2}+k^2+\frac{\omega}{\tilde{D}}}. \tag{94}$$

We will in the following again use the quasistationary approximation of the impurity diffusion equation, which corresponds to dropping the term $\omega/\tilde{D}$ on the RHS of Eq. (94). As discussed before, we are mainly interested in perturbation wavelengths much smaller than the diffusion length. Note that in this limit, and within the quasistationary approximation, we have $\tilde{q}_k\approx|k|$. We will not, however, make use of this simplification for the sake of generality. Next, we linearize the JH formula around the initial spacing λ_0 and the pulling speed v_p:

$$\Delta T_{\mathrm{JH}}(\lambda,v)=\Delta T_{\mathrm{JH}}(\lambda_0,v_p)+\left.\frac{\partial\Delta T_{\mathrm{JH}}}{\partial\lambda}\right|_{\lambda_0,v_p}\lambda_0\frac{\partial y}{\partial x}+\left.\frac{\partial\Delta T_{JH}}{\partial v}\right|_{\lambda_0,v_p}\dot{\xi}, \tag{95}$$

where we have used $v_n=v_p+\dot{\xi}$ and $\lambda-\lambda_0=\lambda_0\partial y/\partial x$ from Eq. (90). The Gibbs-Thomson condition, Eq. (88), linearized in the perturbations, becomes

$$G\xi_k=\tilde{m}\tilde{c}\left(\frac{2}{\tilde{l}}\xi_k-\tilde{b}_k\right)-\left.\frac{\partial\Delta T_{\mathrm{JH}}}{\partial\lambda}\right|_{\lambda_0,v_p}\frac{v_pk^2}{\omega}\xi_k-\left.\frac{\partial\Delta T_{\mathrm{JH}}}{\partial v}\right|_{\lambda_0,v_p}\omega\xi_k. \tag{96}$$

Inserting Eq. (93) for $\tilde{b}_k$ with the quasistationary approximation for $\tilde{q}_k$, and using Eqs. (27) and (28) to calculate the derivatives of ΔT_{JH}, we obtain a quadratic equation for ω. In the dimensionless quantities defined as before, this equation reads

$$\left(\frac{wr}{\tilde{\rho}_0(\kappa)}+\frac{P(\eta)}{2\eta(1-\eta)}\right)\Omega^2-\left(wr-\frac{g}{2}-\frac{2w\,\mathrm{Pe}\,r^2k_E}{\tilde{\rho}_0(\kappa)}\right)\Omega+\frac{2\pi^2P(\eta)}{\eta(1-\eta)}\left(1-\frac{1}{\Lambda^2}\right)\kappa^2=0, \tag{97}$$

with $\tilde{\rho}_0(\kappa)$ defined by Eq. (64). Figure 12 shows a comparison between this formula and the full calculation, Eq. (74), for the same parameters as in Fig. 9. We see that, indeed, all features of the spectrum at small κ are correctly predicted, including the transition from real to complex growth rates with growing κ. This means that the simple calculation outlined above is able to capture the qualitatively new feature of the instability. Formally, the occurrence of the complex growth rates is due to the fact that the equation is quadratic in ω, whereas the analogous equation of the Mullins-Sekerka calculation is linear. This difference arises from the growth constraint resulting from Cahn's hypothesis. Physically, the change in the local lamellar spacing resulting from this constraint counteracts the destabilization of the front by the impurities. This is due to the fact that in a convex (i.e., protruding) part of the front, the growing lamellar spacing leads to an increase in the JH undercooling, whereas the inverse is true for concave parts. The magnitude of this effect is proportional to the slope of the JH undercooling versus spacing curve, which increases with lamellar spacing. The oscillations occur because only the *time derivative* of the spacing depends on the instantaneous front shape, but not the spacing itself. Therefore, the perturbation of the lamellar spacing is phase shifted by $\pi/2$ with respect to the perturbation of the front shape. Consequently, during an oscillation cycle the former has its maximum amplitude when the front is planar. In summary, the long-wavelength oscillations are created by the interplay of the destabilizing effect of the impurity diffusion field, which is the same as for a monophase solidification front, and the dynamical response of the underlying lamellar structure.

B. Inclusion of surface tension

As shown in Fig. 12, the spectrum derived from the stability analysis of the effective interface free boundary problem is in good quantitative agreement with the full spectrum at small κ. This approach, however, fails to predict the restabilization of the interface at larger κ because it lacks capillarity. To add this effect, we can use the insights of Sec. V for the symmetric case, where it was noted that the eutectic stability spectrum could be interpreted as a planar interface spectrum with an effective surface tension. This suggests that we can simply add to the Gibbs-Thomson condition [Eq. (88)] a capillary term proportional to the curvature of the effective interface, which yields the new condition

$$T=T_E-\tilde{m}\tilde{c}-\Delta T_{\mathrm{JH}}(\lambda,v_n)-\Gamma_{\mathrm{eff}}K[\xi], \tag{98}$$

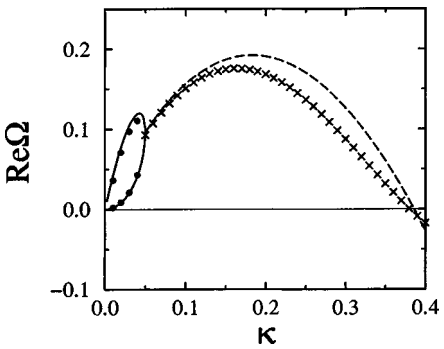

FIG. 13. Comparison between the full calculation and Eq. (104) for an off-eutectic composition (η=0.65). The other parameters are as for Figs. 9 and 12. Symbols, full calculation, Eq. (74) (circles, real modes; crosses, complex modes). Lines, Eq. (97); solid lines, real modes; dashed lines, complex modes.

where $\Gamma_{\rm eff}$ is an effective Gibbs-Thomson coefficient. For the completely symmetric case, we can identify $\Gamma_{\rm eff}$ by comparing Eq. (97) to Eq. (75) with the approximate expressions, Eqs. (76), for the coefficients $a(\kappa)$, $b(\kappa)$, and $c(\kappa)$, which yields at once the expression

$$\Gamma_{\rm eff}=\Gamma_E+\frac{M\Delta c\,{\rm Pe}\,\lambda_0}{4\pi^2}R_0, \tag{99}$$

where $\Gamma_E=\Gamma\cos\theta$ and R_0 is given by Eq. (B11).

Let us now consider the extension of this result to a general alloy phase diagram and an arbitrary composition. The RHS of Eq. (99) contains two contributions that arise from the large-scale bending of the effective interface. The first is, in terms of the discrete formalism, the part of the curvature matrix **K** that is not contained in the JH formula. For arbitrary Gibbs-Thomson constants, contact angles, and volume fractions, simple arguments detailed in Appendix C lead to the conclusion that the reaction of a composite interface to a small curvature can be described by a Gibbs-Thomson constant Γ_E defined by Eq. (C4) that depends on Γ_α, Γ_β, θ_α, θ_β and the volume fraction η.

The second term on the RHS of Eq. (99) originates from the eutectic diffusion field, which was shown in Sec. V to have a stabilizing effect analogous to a supplementary capillary term. For general alloy composition and phase diagram, this contribution can in principle be extracted by expanding the complete spectrum to order κ^2. Since, as noted earlier, calculating this spectrum involves finding the roots of a fourth order polynomial in Ω, this expansion is extremely tedious and was not carried out here. We have found numerically, however, that reasonably accurate predictions can be obtained for off-eutectic compositions if we simply use $\Gamma_{\rm eff}$ defined by Eq. (99) with Γ_E given by Eq. (C4). In view of the large uncertainty in the knowledge of several of the materials' parameters, notably the Gibbs-Thomson constants and the diffusion coefficients, this level of accuracy seems presently sufficient to interpret experimental results. Only very precise experiments could probe the differences between the full calculation and this approximation.

Let us state the final result for the stability spectrum in two different forms to display the analogies with the MS and DL calculations, respectively. First, to compare to the MS instability, the dispersion relation can be written

$$\frac{\omega\tilde{l}^2}{2\tilde{D}}=A(k\tilde{l})\left(1-\frac{\tilde{l}}{2l_T}-\frac{\bar{d}_0}{2\tilde{l}}(k\tilde{l})^2\right)-2k_E - \frac{\tilde{l}A(k\tilde{l})}{4\tilde{m}\Delta\tilde{c}}\Delta T_{\rm min}\left[\left(\Lambda-\frac{1}{\Lambda}\right)\frac{\nu_p k^2}{\omega}+\frac{\omega\Lambda}{\nu_p}\right], \tag{100}$$

where $A(k\tilde{l})$, the thermal length l_T, and the effective capillary length $\bar{d}_0$ are defined by

$$A(k\tilde{l})=\sqrt{1+(k\tilde{l})^2}-1+2k_E, \tag{101}$$

$$l_T=\tilde{m}\Delta\tilde{c}/G, \tag{102}$$

$$\bar{d}_0=\frac{\Gamma_{\rm eff}}{\tilde{m}\Delta\tilde{c}}. \tag{103}$$

Without the eutectic part on the RHS, Eq. (100) is the classical MS result for the one-sided model.

In the dimensionless quantities used by DL, the result is

$$\left(\frac{wr}{\tilde{\rho}_0(\kappa)}+\frac{P(\eta)}{2\eta(1-\eta)}\right)\Omega^2 - \left[wr-\frac{g}{2}-\left(\frac{4\pi^2\gamma(\eta)P(\eta)}{\Lambda^2}+R_0\right)\frac{\kappa^2}{2} - \frac{2w\,{\rm Per}^2k_E}{\tilde{\rho}_0(\kappa)}\right]\Omega+\frac{2\pi^2P(\eta)}{\eta(1-\eta)}\left(1-\frac{1}{\Lambda^2}\right)\kappa^2=0, \tag{104}$$

with the function $\gamma(\eta)$ given by

$$\gamma(\eta)=\frac{\Gamma_E(\eta)(m_\alpha+m_\beta)/2}{(1-\eta)m_\beta\Gamma_\alpha\sin\theta_\alpha+\eta m_\alpha\Gamma_\beta\sin\theta_\beta}. \tag{105}$$

Figure 13 shows both the full calculation and the result of Eq. (104) for the stability spectrum of the symmetric phase diagram at an off-eutectic composition, η=0.65. The two are in reasonably good quantitative agreement, even though the value of R_0 corresponding to η=1/2 was used in Eq. (99).

Let us now briefly indicate which modifications will occur if the two impurity liquidus slopes differ, $\tilde{m}_\alpha\neq\tilde{m}_\beta$. In this case, the eutectic composition depends on the impurity concentration, and there is a eutectic boundary layer with a magnitude depending on the impurity concentration at the interface. If the two diffusion coefficients D and $\tilde{D}$ are equal ($r=1$), all results carry over if we use the liquidus slope $\tilde{M}$ defined by Eq. (5) instead of $\tilde{m}$ in all equations, and redefine the parameter $w=\tilde{M}\Delta\tilde{c}/M\Delta c$. This should usually be a reasonable approximation. If the two diffusion lengths are very different, however, one would have to consider the eutectic boundary layer separately. Then, a separate Fourier expansion has to be used for the eutectic boundary layer, and Eq. (96) is replaced by a more complicated form containing both diffusion lengths.

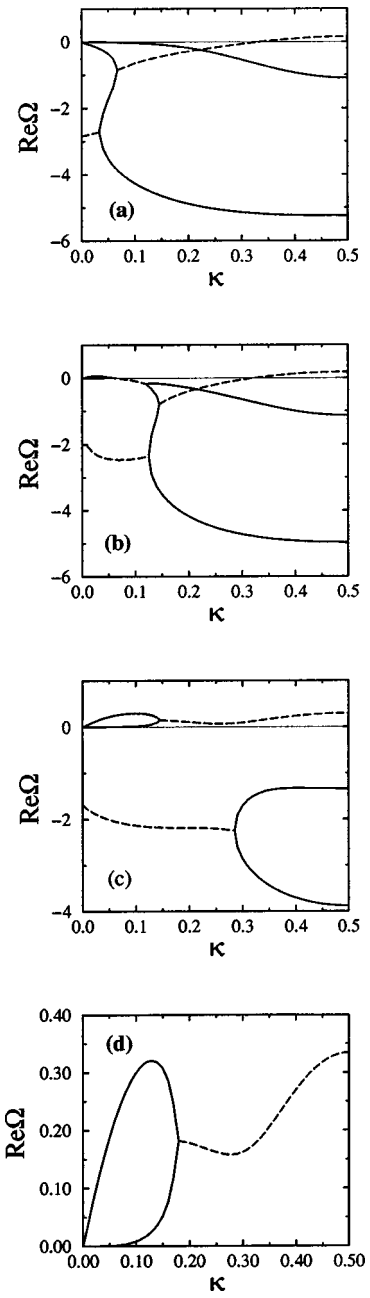

FIG. 14. Stability spectra for $\eta=0.75$, $\Lambda=1$, $\theta=45°$, $k_E=0.05$, and (a) $g=0$, $w=0$; (b) $g=0$, $w=0.01$; (c) $g=0$, $w=0.05$; and (d) $g=0.05$, $w=0.1$. In (d) only the unstable branch is shown.

VII. SHORT-WAVELENGTH MODES

Up to now, we have only considered the instabilities arising from the diffusive and MS modes. Let us now turn to the effect of the ternary impurity on the 2λ-oscillatory (2λ-O) instability at off-eutectic compositions. In Fig. 14, we show a series of spectra at an off-eutectic composition ($\eta=0.8$) with increasing impurity concentration. The first spectrum, without impurity, again reproduces one of DL's figures. The diffusive branch is completely stable, but there is an unstable complex branch, with the most unstable mode at $\kappa=0.5$. For a small impurity concentration ($w=0.01$), the long-wavelength morphological instability is simultaneously present, but the structure of the spectrum stays qualitatively unchanged. For still higher impurity concentration ($w=0.05$), however, the spectrum becomes quite different: a single branch of the spectrum now contains both the long- and short-wavelength instabilities, making their distinction somewhat arbitrary, whereas the other branch is completely stable. We have always found a similar structure for impurity concentrations larger than $w\approx 0.02$. Figure 14(d) shows only the unstable branch for $g=0.05$, $w=0.1$, and $\Lambda=1$, for a comparison with the spectrum at the eutectic composition shown in Fig. 6(b). The long-wavelength part of the two spectra is very similar, but at the off-eutectic composition the most unstable mode is the 2λ-O mode. The growth rates of the long- and short-wavelength instabilities, however, are not very different, and we can expect a competition between the two.

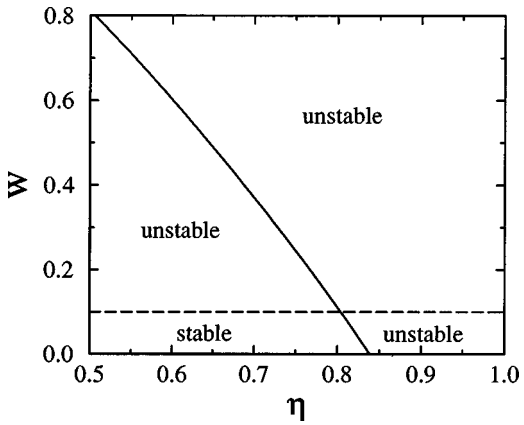

FIG. 15. Stability diagram for the symmetric eutectic alloy in the space (η,w) for $\Lambda=1$, $g=0.2$, $\mathrm{Pe}=0.01$, and $k_E=0.05$. Solid line, neutral stability limit for the 2λ-O mode. Dashed line, constitutional supercooling criterion.

At $\kappa=0.5$, the matrix elements of **A** become real. The characteristic equation can again be factored in two quadratic equations, which are simply

$$\mathbf{A}^{\alpha,\alpha}=0 \quad \text{and} \quad \mathbf{A}^{\beta,\beta}=0. \tag{106}$$

This allows us, in particular, to obtain an equation for the neutral stability boundaries where the 2λ-O mode first becomes unstable. For the model alloy with the symmetric phase diagram, we have on the α-rich side of the phase diagram ($\eta>0.5$)

$$g=2wr-\frac{wr}{\eta}2k_E r\,\mathrm{Pe}\,\tilde{S}_1(0.5,\eta)+2\eta-1 + \frac{2}{\eta}\left(R_2(\eta)-S_3(0.5,\eta)-\frac{2\cot\theta}{\Lambda^2}P(\eta)\right), \tag{107}$$

where $R_2(\eta)$ and $S_3(\kappa,\eta)$ are defined in appendix A. This is a direct generalization of DL's result for the binary eutectic. Figure 15 shows the resulting stability diagram for $g=0.2$ and $\Lambda=1$. The dashed line is the constitutional supercooling criterion, and the long-range instability is present everywhere above this line. The solid line was calculated using Eq. (107), and the 2λ-O mode is unstable to the right of this line. We see that when the impurity concentration increases, the range in volume fraction for which the eutectic front is stable decreases. This means that, not surprisingly, the ter-

nary impurity boundary layer enhances the oscillatory instability. Furthermore, there is a large region in parameter space where the two instabilities compete and the fastest growing linear mode needs to be identified from a plot of the spectrum.

VIII. CONCLUSION

We have performed a linear stability analysis of a thin lamellar eutectic interface in the presence of a ternary impurity to investigate the initial stages of colony formation. The extension of Datye and Langer's method has allowed us to calculate the complete stability spectrum of the steady-state interface. From previous numerical studies of the binary eutectic case [21], we expect this discrete stability analysis to be quantitatively accurate for spacings near the JH minimum undercooling spacing $\lambda_{\min}$.

The most dramatic conclusion resulting from our analysis is that the morphological instability of the eutectic interface induced by the ternary impurity is oscillatory, in contrast to the standard MS instability of a planar interface for a dilute binary alloy, which is nonoscillatory. We have seen that oscillatory modes originate from the interplay between the diffusive instability driven by the ternary impurity and the ''dynamical feedback'' of the local change in lamellar spacing on the front motion. In a transient regime, these modes should create oscillatory microstructures with a wavelength of several lamellar spacings, such as the ones displayed in Fig. 10. There indeed seems to be recent experimental evidence for large-scale oscillatory structures of this type in a transparent organic with a dilute ternary impurity [33], but a more detailed comparison between theory and experiment is now needed.

Aside from its oscillatory character, the morphological instability of the eutectic interface is qualitatively similar, near onset, to the standard MS instability of a monophase front. In particular, we find that the expressions for the critical onset velocity and morphological instability wavelength are analogous to those for the classic Mullins-Sekerka instability of a planar interface. The main difference is that the restabilization of the interface at short wavelength is controlled by an effective surface tension that depends on the geometry of the lamellar interface and on interlamellar diffusion, which has a restabilizing effect. One consequence of this result is that the constitutional supercooling criterion that has been commonly used in the metallurgical literature to predict the onset of instability is indeed applicable for typical alloy compositions. Note, however, that this criterion becomes inaccurate for very small concentrations of the ternary impurity.

Above the onset of instability, the stability spectrum can exhibit both real and complex modes. The scaling of the wavelength of the fastest growing mode with pulling velocity depends on the nature of the mode. For complex modes, far above the onset this wavelength scales as the geometric mean of the capillary length and the diffusion length. For real modes, the situation is more complicated. In both cases, for fixed velocity and lamellar spacing, the wavelength far above the onset and at sufficiently high impurity concentration scales as the inverse square root of the impurity concentration. Note that all these statements concern the *primary instability* of the eutectic front and not the finally selected colony spacing. After the first colonies have formed, the nonplanar front may undergo a complicated sequence of cell elimination or tip splitting events, as during the development of monophase cellular structures.

Furthermore, we have shown that the eutectic front dynamics on scales much larger than the lamellar spacing can be formulated as a free boundary problem with a modified Gibbs-Thomson condition that is coupled to a slow evolution equation for the lamellar spacing. This formulation provides a deeper physical understanding of the eutectic front dynamics on this scale. In addition, we have shown that it can be used to calculate an approximate stability spectrum that is well suited to interpret experimental data. The effective capillary length appearing in this spectrum contains contributions both from an averaging over the material properties of the two phases, weighted by geometric factors, and from the eutectic interlamellar diffusion field, which acts as a stabilizing force.

Finally, we have found that the short-wavelength oscillatory instability, already present in a binary eutectic, is enhanced by the ternary impurity boundary layer. This reduces the composition range for stable lamellar eutectic growth, even below constitutional supercooling. Above constitutional supercooling and for sufficiently off-eutectic compositions, the long-range and 2λ-oscillatory instabilities are both present and may compete with each other.

In conclusion, we have shown that the instability of a lamellar eutectic interface in the presence of a ternary impurity is in some respects similar to the Mullins-Sekerka instability of a dilute binary alloy, but also presents striking differences. There are two interesting future prospects. First, dynamical simulations of the complete equations of motion are necessary to go beyond this linear stability analysis and to investigate the subsequent stages of the instability, as well as to determine what structures are ultimately formed. Work on these issues using the phase-field method is currently in progress. Second, it seems worthwhile to extend the effective interface approach to a nonlinear regime to model the shape and dynamics of fully developed colonies, as depicted in Fig. 1.

ACKNOWLEDGMENTS

We thank S. Akamatsu and G. Faivre for many fruitful discussions and for sharing with us their unpublished experimental results. This research was supported by the U.S DOE under Grant No. DE-FG02-92ER45471.

APPENDIX A: SUMMARY OF DATYE AND LANGER'S RESULTS

We will state here DL's results for the matrices **G**, **K**, and **U** and transform them into our notations. The matrix **G** can be simply read off the definitions of the average interface positions $\langle \xi \rangle_j^s$; Eqs. (38), and of the Fourier expansion, Eq. (41):

$$\mathbf{G} = \frac{G}{2}\begin{pmatrix} 1 & 1 \\ e^{ik\lambda} & 1 \end{pmatrix}. \tag{A1}$$

The curvature matrix contains two contributions. The first arises from the change in the local lamellar spacing due to the horizontal displacements y_j^s. The second appears when the interface is bent on a scale of several lamellae. Then, the trijunction points are turned by small angles with respect to their steady-state orientation. These angles can be related to the time derivatives of the horizontal displacements. Finally, we use the growth constraints, Eq. (40), and obtain

$$\mathbf{K}^{\alpha,\alpha}=\frac{2ie^{ik\lambda/2}\sin(k\lambda/2)}{\lambda^2}\left(\frac{2v_p\sin\theta_\alpha}{\omega\lambda\eta^2}-\frac{\cos\theta_\alpha}{\eta}\right), \quad \text{(A2)}$$

$$\mathbf{K}^{\beta,\beta}=\frac{2ie^{ik\lambda/2}\sin(k\lambda/2)}{\lambda^2}\left(\frac{2v_p\sin\theta_\beta}{\omega\lambda(1-\eta)^2}-\frac{\cos\theta_\beta}{1-\eta}\right), \quad \text{(A3)}$$

$$\mathbf{K}^{\alpha,\beta}=\mathbf{K}^{\alpha,\alpha*}, \quad \text{(A4)}$$

$$\mathbf{K}^{\beta,\alpha}=e^{ik\lambda}\mathbf{K}^{\beta,\beta*}, \quad \text{(A5)}$$

where the asterisks in the last two equations denote complex conjugation of all the coefficients, but not ω.

For the symmetric phase diagram, we may conveniently rewrite this matrix in the dimensionless parameters defined in Sec. IV. We remark that in this case we have

$$\lambda_{\min}^2=\frac{l\Gamma\sin\theta}{M\Delta cP(\eta)}. \quad \text{(A6)}$$

This relation can be used to eliminate $\sin\theta$ in the matrix; the reduced lamellar spacing Λ appears, and, for example, we obtain for $\mathbf{K}^{\alpha,\alpha}$

$$\mathbf{K}^{\alpha,\alpha}=2ie^{i\pi\kappa}\sin(\pi\kappa)\frac{M\Delta cP(\eta)}{l\Lambda^2\Gamma}\left(\frac{2}{\Omega\eta^2}-\frac{\cot\theta}{\eta}\right). \quad \text{(A7)}$$

Note that in the general case the scaling with respect to the physical parameters would remain the same; however, additional coefficients depending on the angles θ_α and θ_β and the liquidus slopes m_α and m_β would appear.

For the matrix $\mathbf{U}$, we will just state DL's results; for more details, see [22]. The calculation is straightforward but tedious because we have to treat the interlamellar diffusion. This brings in various sums over the Fourier modes of the steady-state expansion, Eq. (12). We define

$$\Delta_\alpha=B_0+u_\infty-u_\alpha, \quad \text{(A8)}$$

$$\Delta_\beta=u_\beta-B_0-u_\infty, \quad \text{(A9)}$$

$$R_1(\eta)=\sum_{n=1}^{\infty}\frac{\sin(2\pi\eta n)}{(\pi n)^2}, \quad \text{(A10)}$$

$$R_2(\eta)=\sum_{n=1}^{\infty}\frac{2\sin^2(\pi\eta n)}{(\pi n)^2}, \quad \text{(A11)}$$

$$\rho_n(\kappa)=\sqrt{4\pi^2(n+\kappa)^2+\mathrm{Pe}^2}-\mathrm{Pe}, \quad \text{(A12)}$$

$$S_1(\kappa,\eta)=\sum_{n=-\infty}^{\infty}\frac{\sin^2[\pi\eta(n+\kappa)]}{\pi^2(n+\kappa)^2\rho_n(\kappa)}, \quad \text{(A13)}$$

$$S_2(\kappa,\eta)=\sum_{n=-\infty}^{\infty}e^{-i\pi(n+\kappa)}\times\frac{\sin[\pi\eta(n+\kappa)]\sin[\pi(1-\eta)(n+\kappa)]}{\pi^2(n+\kappa)^2\rho_n(\kappa)}, \quad \text{(A14)}$$

$$S_3(\kappa,\eta)=4\sum_{m=-\infty}^{\infty}\frac{\sin[\pi\eta(m+\kappa)]}{\pi(m+\kappa)\rho_m(\kappa)}\times\sum_{n=-\infty;\neq0}^{\infty}\frac{|n|}{n}\sin(\pi\eta n)e^{i\pi(n-m-\kappa)/2}\times\frac{\sin[\pi(n-m-\kappa)/2]}{\pi(n-m-\kappa)}, \quad \text{(A15)}$$

$$S_4(\kappa,\eta)=\sum_{n=-\infty}^{\infty}e^{i\pi\eta(n+\kappa)}\frac{\sin[\pi\eta(n+\kappa)]}{\pi(n+\kappa)\rho_n(\kappa)}. \quad \text{(A16)}$$

Using these quantities, the matrix elements of $\mathbf{U}$ are

$$\mathbf{U}^{\alpha,\alpha}=\frac{1}{l}\left(\Omega U_1^\alpha(\kappa,\eta)+U_2^\alpha(\kappa,\eta)+\frac{2ie^{i\pi\kappa}}{\Omega}\sin(\pi\kappa)U_3(\kappa,\eta)\right), \quad \text{(A17)}$$

$$\mathbf{U}^{\beta,\beta}=\frac{-1}{l}\left(\Omega U_1^\beta(\kappa,\eta)+U_2^\beta(\kappa,\eta)+\frac{2ie^{i\pi\kappa}}{\Omega}\sin(\pi\kappa)U_3(\kappa,1-\eta)\right), \quad \text{(A18)}$$

$$\mathbf{U}^{\alpha,\beta}=\mathbf{U}^{\alpha,\alpha*}, \quad \text{(A19)}$$

$$\mathbf{U}^{\beta,\alpha}=e^{ik\lambda}\mathbf{U}^{\beta,\beta*}, \quad \text{(A20)}$$

with

$$U_1^\alpha(\kappa,\eta)=\frac{1}{\eta}[\Delta_\alpha S_1(\kappa,\eta)-\Delta_\beta S_2^*(\kappa,\eta)], \quad \text{(A21)}$$

$$U_1^\beta(\kappa,\eta)=\frac{1}{1-\eta}[\Delta_\beta S_1(\kappa,1-\eta)-\Delta_\alpha S_2^*(\kappa,1-\eta)], \quad \text{(A22)}$$

$$U_2^\alpha(\kappa,\eta)=-B_0+\frac{1}{\eta}[S_3^*(\kappa,\eta)-R_2(\eta)], \quad \text{(A23)}$$

$$U_2^\beta(\kappa,\eta)=B_0+\frac{1}{(1-\eta)}[S_3^*(\kappa,1-\eta)-R_2(1-\eta)], \quad \text{(A24)}$$

$$U_3(\kappa,\eta)=\frac{1}{\eta}[2P(\eta)/\eta-R_1(\eta)-2S_4^*(\kappa,\eta)]. \quad \text{(A25)}$$

APPENDIX B: LIMIT OF THE DL SUMS FOR $\kappa \to 0$

For the detailed study of the symmetric phase diagram at eutectic composition, we need to know the leading order behavior of the functions U_1^α, U_2^α, and U_3, for $\kappa \to 0$. To this end, we have to expand the sums S_n in κ and resum the resulting terms. We will systematically neglect terms of relative magnitude Pe, as was already done in DL's calculations leading to the results of the preceding appendix.

We have to single out terms containing the function $\rho_0(\kappa)$ in the denominator, because these terms will be singular in the limit $\kappa \to 0$. To see this, note that we have

$$\rho_0(\kappa) = \begin{cases} 2\pi^2\kappa^2/\mathrm{Pe} + O(\kappa^4) & \text{for } 2\pi\kappa \ll \mathrm{Pe}, \\ 2\pi|\kappa| & \text{for } 2\pi\kappa \gg \mathrm{Pe}. \end{cases} \tag{B1}$$

We will be interested in a regime where the wavelength of the perturbation is larger than the lamellar spacing, but much smaller than the diffusion length; hence the latter limit applies.

Similarly, the function $\tilde{\rho}_0(\kappa)$ will become small when κ tends to 0:

$$\tilde{\rho}_0(\kappa) = \begin{cases} r\,\mathrm{Pe}\,k_E + 2\pi^2\kappa^2/\mathrm{Pe} + O(\kappa^4), & 2\pi\kappa \ll \mathrm{Pe}, \\ 2\pi|\kappa|, & 2\pi\kappa \gg \mathrm{Pe}. \end{cases} \tag{B2}$$

Hence the terms proportional to $\tilde{\rho}_0^{-1}$ in the impurity contributions have to be considered separately.

Expanding $S_1(\kappa,\eta)$ and $S_2(\kappa,\eta)$, we obtain

$$S_1(\kappa,\eta) = \frac{\eta^2 - \frac{1}{3}\eta^4\pi^2\kappa^2}{\rho_0(\kappa)} + P(\eta) + [\eta^2 R_3(\eta) - 3\eta R_4(\eta) + 6R_5(\eta)]\pi^2\kappa^2 + O(\kappa^4/\rho_0) + O(\kappa^4), \tag{B3}$$

$$S_2(\kappa,\eta) = \left\{1 - i\pi\kappa - \frac{1}{2}\left[1 + \frac{1}{3}(\eta^2 + (1-\eta)^2)\right]\pi^2\kappa^2\right\} \times \frac{\eta(1-\eta)}{\rho_0(\kappa)} - (1 - i\pi\kappa - \pi^2\kappa^2)P(\eta) + [\eta(1-\eta)R_3(\eta) + 3(\eta - 1/2)R_4(\eta) - 6R_5(\eta)]\pi^2\kappa^2 + O(\kappa^4/\rho_0) + O(\kappa^4), \tag{B4}$$

with

$$R_3(\eta) = \sum_{n=1}^{\infty} \frac{\cos 2\pi\eta n}{(\pi n)^3}, \tag{B5}$$

$$R_4(\eta) = \sum_{n=1}^{\infty} \frac{\sin 2\pi\eta n}{(\pi n)^4}, \tag{B6}$$

$$R_5(\eta) = \sum_{n=1}^{\infty} \frac{\sin^2 \pi\eta n}{(\pi n)^5}. \tag{B7}$$

The expansions for the impurity sums $\tilde{S}_1(\kappa,\eta)$ and $\tilde{S}_2(\kappa,\eta)$ are obtained by replacing $\rho_0(\kappa)$ by $\tilde{\rho}_0(\kappa)$ in the above expressions.

With the help of these expressions and the definition of U_1^α, we find for $\eta = 1/2$ and $\Delta_\alpha = \Delta_\beta = 1/2$,

$$\mathrm{Re}[e^{-i\pi\kappa/2}U_1^\alpha(\kappa,1/2)] = 2P(1/2) + [12R_5(1/2) - \tfrac{3}{4}P(1/2)]\pi^2\kappa^2 + O(\kappa^4). \tag{B8}$$

Rather remarkably, all the singular terms cancel out. A comparison with direct numerical summation shows that the limit behavior is correct and that the neglected terms sum up to a correction that does not exceed $P(1/2)$, even for large values of κ.

For the impurities, we need the expression

$$\tilde{S}_1(\kappa,1/2)\cos\frac{\pi\kappa}{2} + \mathrm{Re}[e^{-i\pi\kappa/2}\tilde{S}_2^*(\kappa,1/2)] = \frac{1 - 5\pi^2\kappa^2/24}{2\tilde{\rho}_0(\kappa)} + \frac{1}{2}[P(1/2) + R_3(1/2)]\pi^2\kappa^2 + O(\kappa^4/\tilde{\rho}_0) + O(\kappa^4). \tag{B9}$$

We will simplify our task for the function U_2^α, which contains the most difficult sum $S_3(\kappa,\eta)$, by directly expanding the product $e^{i\pi\kappa/2}S_3(\kappa,1/2)$. Using $B_0 = 0$ for the symmetric phase diagram at eutectic composition, we obtain

$$\mathrm{Re}(e^{i\pi\kappa/2}U_2^\alpha) = R_0\kappa^2/2 + O(\kappa^4), \tag{B10}$$

with

$$R_0 = 2\pi^2\left[3R_6(1/2) - \frac{1}{6}R_2(1/2) - R_7(1/2)\right] \approx 0.4965, \tag{B11}$$

$$R_6(\eta) = \sum_{n=1}^{\infty} \frac{2\sin(\pi\eta n)}{(\pi n)^4}, \tag{B12}$$

$$R_7(\eta) = \sum_{m=1}^{\infty} \frac{2\sin(\pi\eta m)}{(\pi m)^2} \sum_{n=-\infty;\neq 0;\neq m}^{\infty} \frac{|n|}{n}\sin(\pi\eta n) \times \frac{\cos^2[\pi(n-m)/2]}{\pi^2(n-m)^2}. \tag{B13}$$

Comparison to direct summation shows that the expression (B10) is accurate to within 5% over the whole range of κ.

Finally, to express U_3, we need the expansion

$$S_4(\kappa,\eta) = \frac{\eta + i\pi\eta^2\kappa}{\rho_0(\kappa)} - \frac{2\pi^2\eta^3\kappa^2 + i\pi^3\eta^4\kappa^3}{3\rho_0(\kappa)} + R_1(\eta)/2 + 2\pi i[P(\eta) - \eta R_1(\eta)]\kappa + [6R_4(\eta) - 8\eta R_3(\eta) - \eta^2 R_1(\eta)]\pi^2\kappa^2/4 + O(\kappa^3). \tag{B14}$$

For Eq. (74), we need

$$2\sin(\pi\kappa)\mathrm{Re}[ie^{i\pi\kappa/2}U_3(\kappa,1/2)] = 8\pi^2 P(\eta)\kappa^2 + O(\kappa)^4. \tag{B15}$$

Collecting all these results, we can finally write down the complete expressions for the coefficients $a(\kappa)$, $b(\kappa)$, and $c(\kappa)$ of Eq. (75) up to order κ^2:

$$a(\kappa)=2P(1/2)+[12R_5(1/2)-\tfrac{3}{4}P(1/2)]\pi^2\kappa^2 + wr\left\{\frac{1-5\pi^2\kappa^2/24}{\tilde{\rho}_0(\kappa)}+[P(1/2)+R_3(1/2)]\pi^2\kappa^2\right\} \tag{B16}$$

$$b(\kappa)=(wr-g/2)(1-\pi^2\kappa^2/8)-\left(\frac{2\pi^2P(1/2)\cot\theta}{\Lambda^2}+\frac{R_0}{2}\right)\kappa^2 - 2w\,\mathrm{Pe}\,r^2k_E\left\{\frac{1-5\pi^2\kappa^2/24}{\tilde{\rho}_0(\kappa)} +[P(1/2)+R_3(1/2)]\pi^2\kappa^2\right\}, \tag{B17}$$

$$c(\kappa)=8\pi^2P(1/2)\left(1-\frac{1}{\Lambda^2}\right)\kappa^2. \tag{B18}$$

To obtain the expressions given by Eqs. (76), we remark that for small κ we can neglect most of the terms listed above. We have to be careful, however, to keep track of all physical effects. For example, formally the leading order term in $a(\kappa)$ is of order κ^{-1} if we use $\tilde{\rho}_0(\kappa)=2\pi|\kappa|$. But this term comes with a prefactor w, proportional to the impurity concentration, whereas the leading order term in the expansion of U_1^α, arising from the eutectic diffusion field, is independent of w. Hence for the approximation to be valid for arbitrary w, we need to keep both terms leading to Eq. (76a) for $a(\kappa)$. Similarly, in $b(\kappa)$, we need to keep the dominant terms for *each* physical effect, even if their order is higher than other terms we may neglect. In particular, we must keep the capillary term that is of order κ^2 and has a prefactor of order unity. Let us show that, at the onset of instability, we can indeed neglect other terms of order κ and κ^2. Keep in mind that we are interested in a regime where κ is small, but not *too* small; a plausible estimate is $\kappa\approx0.01$. First, there is the correction $-\pi^2\kappa^2(wr-g/2)/8$ to the constitutional supercooling criterion, of order κ^2. But as $wr-g/2$ is very small near the onset, this term is actually much smaller than the capillary term. Next, there are terms of orders κ and κ^2 arising from the impurity contribution. But all of these come with a prefactor of $w\,\mathrm{Pe}\,k_E$; as both w and Pe are small quantities and $k_E<1$, it seems justified to neglect them. For example, for $w=0.1$, $\mathrm{Pe}=0.01$, and $\kappa=0.01$, the largest neglected term is of order $w\,\mathrm{Pe}\kappa\sim10^{-5}$, whereas the capillary term is of order $\kappa^2\sim10^{-4}$. Hence, Eq. (76b) for $b(\kappa)$ seems well justified at the onset of instability.

APPENDIX C: EFFECTIVE SURFACE TENSION

We will give here an expression for the Gibbs-Thomson constant of a lamellar eutectic interface Γ_E that describes the shift of the average interface temperature when the composite interface is curved on a scale much larger than the lamellar spacing. This analysis is necessary because, in a composite material, the interface with the weaker surface tension will absorb more of the curvature, leading to an effective surface tension, that depends on the volume fraction. Note that the expression derived here is valid in thermodynamic equilibrium and contains only the ''geometric part'' of the effective Gibbs-Thomson constant Γ_{eff} for a *moving* eutectic front, in which the stabilizing effect of the interlamellar diffusion has to be included.

Consider a lamellar interface that is curved such that the $\alpha\beta$ solid-solid interfaces on the two sides of a lamella pair make a small angle ϕ. Suppose that the $\beta\alpha$ interface between them is turned by an angle ϕ_1. The corrections of the curvature with respect to the planar front values are then given by (using the fact that $\phi\approx\lambda/R$ for large radii of curvature R)

$$\delta K_\alpha=\frac{\cos\theta_\alpha}{\eta\lambda}\phi_1 \quad\text{and}\quad \delta K_\beta=\frac{\cos\theta_\beta}{(1-\eta)\lambda}(\phi-\phi_1). \tag{C1}$$

As the average temperature of neighboring lamellae should be the same, we must have

$$\delta K_\alpha\Gamma_\alpha=\delta K_\beta\Gamma_\beta. \tag{C2}$$

From this condition, we can determine the unknown angle ϕ_1. Finally, we obtain the undercooling of the interface as

$$\Delta T=\Gamma_E K \tag{C3}$$

with

$$\Gamma_E=\frac{\Gamma_\alpha\Gamma_\beta\cos\theta_\alpha\cos\theta_\beta}{(1-\eta)\Gamma_\alpha\cos\theta_\alpha+\eta\Gamma_\beta\cos\theta_\beta}. \tag{C4}$$

[1] H. W. Weart and D. J. Mack, Trans. Metall. Soc. AIME **212**, 664 (1958).
[2] J. P. Chilton and W. C. Winegard, J. Inst. Met. **89**, 162 (1961).
[3] R. W. Kraft and D. L. Albright, Trans. Metall. Soc. AIME **221**, 95 (1961).
[4] J. D. Hunt and K. A. Jackson, Trans. Metall. Soc. AIME **236**, 843 (1966).
[5] J. E. Gruzleski and W. C. Winegard, J. Inst. Met. **96**, 304 (1968); Trans. Metall. Soc. AIME **242**, 1785 (1968).
[6] W. M. Rumball, Metallurgia **78**, 141 (1968).
[7] P. K. Rohatgi and C. M. Adams, Trans. Metall. Soc. AIME **245**, 1609 (1969).
[8] J. B. Bullock, C. J. Simpson, J. A. Eady, and W. C. Winegard, J. Inst. Met. **99**, 212 (1971).
[9] M. D. Rinaldi, R. M. Sharp, and M. C. Flemings, Metall. Trans. A **3**, 3133 (1972).
[10] W. W. Mullins and R. F. Sekerka, J. Appl. Phys. **3**, 444 (1964).
[11] W. A. Tiller, in *Liquid Metals and Solidification* (American Society of Metals, Cleveland, 1958).
[12] W. H. Brandt, J. Appl. Phys. **16**, 139 (1945).
[13] C. Zener, Trans. Metall. Soc. AIME **167**, 550 (1946).
[14] M. Hillert, Jernkontorets Ann. **141**, 773 (1957).
[15] K. A. Jackson and J. D. Hunt, Trans. Metall. Soc. AIME **236**,

1129 (1966).
[16] R. Trivedi and W. Kurz, in *Solidification Processing of Eutectic Alloys*, edited by D. M. Stefanescu, G. J. Abbaschian, and R. J. Bayuzick (The Metallurgical Society, Montreal, 1988).
[17] H. E. Cline, Trans. Metall. Soc. AIME **262**, 1613 (1968).
[18] D. T. J. Hurle and E. Jakeman, J. Cryst. Growth **3**, 574 (1968).
[19] S. Strassler and W. R. Schneider, Phys. Condens. Matter **17**, 153 (1974).
[20] H. E. Cline, J. Appl. Phys. **50**, 4780 (1979).
[21] A. Karma and A. Sarkissian, Metall. Trans. A **27**, 635 (1996).
[22] V. Datye and J. S. Langer, Phys. Rev. B **24**, 4155 (1981).
[23] J. S. Langer, Phys. Rev. Lett. **44**, 1023 (1980).
[24] A. Karma, Phys. Rev. Lett. **59**, 71 (1987).
[25] A. Sarkissian, Ph.D. thesis, Northeastern University, Boston, 1994 (unpublished).
[26] K. Kassner and C. Misbah, Phys. Rev. A **44**, 6533 (1991).
[27] G. Faivre and J. Mergy, Phys. Rev. A **45**, 7320 (1992); **46**, 963 (1992).
[28] M. Ginibre, S. Akamatsu, and G. Faivre, Phys. Rev. E **56**, 780 (1997).
[29] D. G. McCartney, J. D. Hunt, and R. M. Jordan, Metall. Trans. A **11**, 1243 (1980).
[30] A. Karma and P. Pelcé, Phys. Rev. A **39**, 4162 (1989); **41**, 6741 (1990).
[31] P. Kopczynski, W.-J. Rappel, and A. Karma, Phys. Rev. Lett. **77**, 3387 (1996).
[32] M. Georgelin and A. Pocheau, Phys. Rev. Lett. **77**, 2698 (1996).
[33] S. Akamatsu and G. Faivre (unpublished results).
[34] S. Akamatsu and G. Faivre, J. Phys. I **6**, 503 (1996).